

Kinematic modelling of neotectonics in the Persia–Tibet–Burma orogen

Zhen Liu* and Peter Bird

Department of Earth and Space Sciences, University of California, Los Angeles, CA 90095-1567, USA. E-mail: zliu@jpl.nasa.gov

Accepted 2007 October 1. Received 2007 September 20; in original form 2007 January 23

SUMMARY

We apply a new kinematic modelling technique (program NeoKinema) to estimate neotectonic flow in the Persia–Tibet–Burma orogen. The models fit geodetic benchmark velocities, geological fault slip rates and stress directions (seismic moment tensor orientations) using a weighted-least-squares method. Models predict long-term velocities, anelastic strain rates and preferred fault slip rates averaged over timescales of 10^4 – 10^6 yr. While we find a few regions of low anelastic strain rate, the mean continuum strain rate in the preferred model is $2.2 \times 10^{-16} \text{ s}^{-1}$ (0.7 per cent Ma^{-1}), so the India-Eurasia collision should not be modelled as an interaction between rigid microplates. For most faults, preferred fault slip rates agree with geological slip rates within their uncertainty bounds; this suggests that deformation imaged by geodesy over tens of years is consistent with deformation over 10^4 – 10^6 yr (given appropriate elastic corrections). We also calculate maps of long-term-average seismicity rate based on model fault slip rates and anelastic strain rates in the continuum, using the seismicity parameters of most comparable type of plate boundary. The pattern is generally in agreement with actual $m > 5.67$ earthquakes in the CMT catalogue (1977–2002), except that the Himalayan front, High Zagros and Altyn Tagh zones have been quieter than predicted. The spatial integral of our forecast over the orogen is $371 m > 5.67$ earthquakes/25.75 yr, versus 238 which actually occurred. If this discrepancy has high significance, it means that some step(s) in our forecast method are faulty (such as the assumption of equal coupled seismogenic thickness in all continental convergent boundaries). If it is only an artefact of stochastic time-dependence, then this may have occurred in the orogen, in the external calibration region, or in both. Independent evidence suggests that large earthquakes (with many aftershocks) will occur along the Himalayan front in the future, possibly reducing this discrepancy.

Key words: Seismicity and tectonics; Intra-plate processes; Neotectonics; Kinematics of crustal and mantle deformation; High strain deformation zones.

1 INTRODUCTION

One important step in understanding complex plate boundary zones is to map their long-term tectonic flow. Over the past decade, the NUVEL1-A plate motion model (DeMets *et al.* 1994) has been widely used to describe relative motion between the 14 largest rigid plates. New data about plate boundaries, seafloor spreading, fault systems, global topography, earthquake moment tensors and geodesy have made possible an updated global plate model: Bird (2003) integrated data from geodesy, bathymetry and/or seismicity and proposed plate boundary model PB2002, in which the globe is divided into 52 rigid plates and 13 orogens. The deformation within each orogen is diffusive and complicated, requiring a local modelling study.

*Now at: Jet Propulsion Laboratory, California Institute of Technology, Pasadena, CA 91109-8099, USA.

Fig. 1 shows the tectonic setting of the Persia–Tibet–Burma orogen, which is the largest orogen in the PB2002 model. It spans eastern Turkey, the northern Middle East, central and southeastern Asia, covering the central and eastern parts of the Alpine–Himalayan mountain belt. Along its southern boundary the Arabia and India Plates collide with the Eurasia Plate, resulting in fold/thrust belts in the Zagros Mountains and the margins of the Tibetan plateau. Abundant earthquakes and fault scarps indicate active deformation in the region. Some heavily populated countries (e.g. China, India, Iran, etc.) lie in the orogen. Historically, large earthquakes have stricken the region and caused catastrophic loss. Therefore, a good assessment of long-term seismicity could be very helpful for loss reduction.

Neotectonic deformation in the Persia–Tibet–Burma orogen has been controversial. For example, in the Tibet Plateau and East Asia, available models include some that are ‘block-like’ (Armijo *et al.* 1989; Avouac & Tapponnier 1993; Peltzer & Saucier 1996; Meade

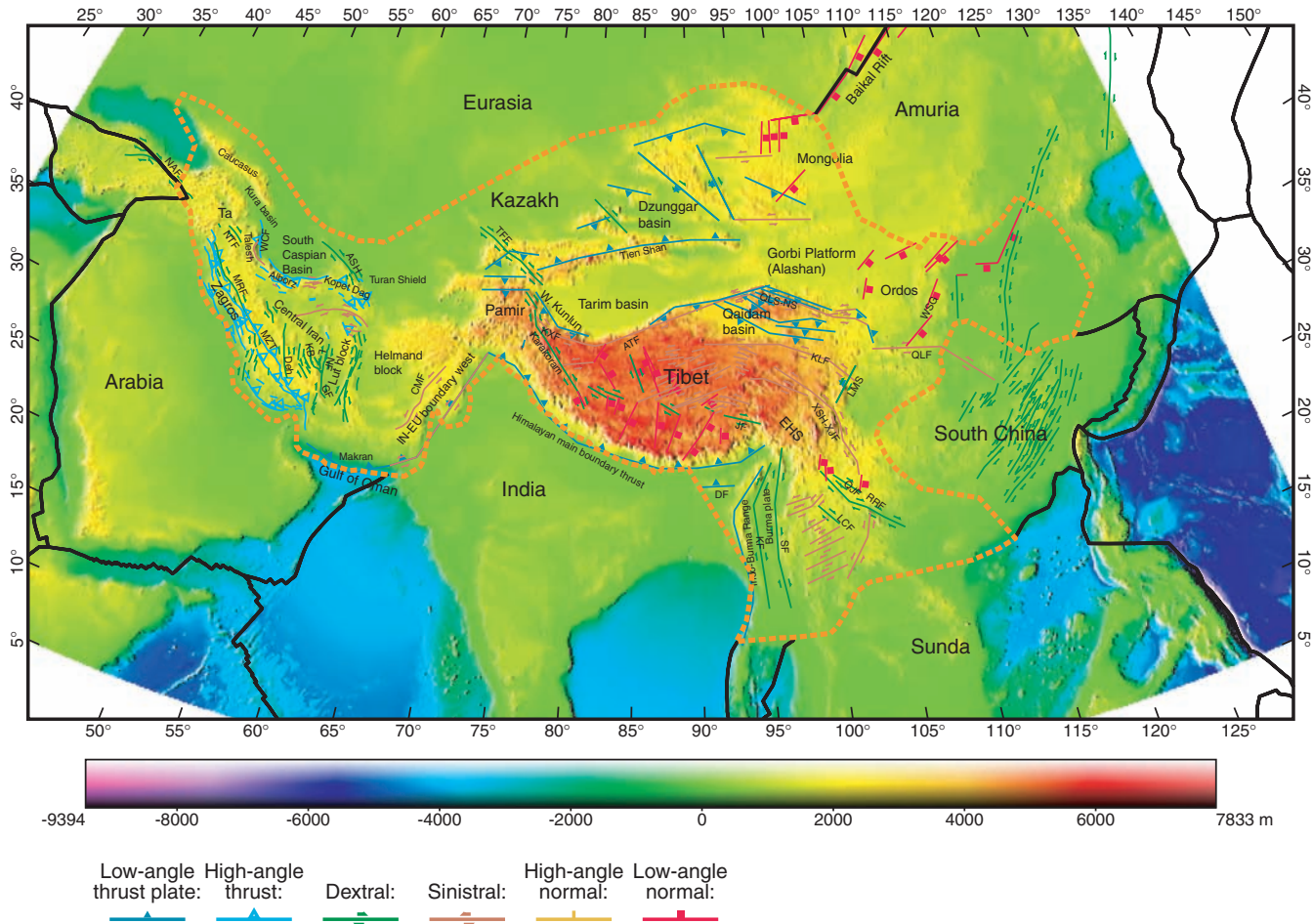


Figure 1. Surface topography and major faults in and around the Persia–Tibet–Burma orogen (heavy dashed curve). Oblique Mercator projection on great circle passing E–W through (84°E, 35°N). Topography data from ETOPO5. Fault traces are from Holt *et al.* (2000) and Berberian & Yeats (2001). Active faults are represented by thin lines. Symbols on the fault traces and colours represent fault type: open triangle and light blue trace = high-angle thrust fault; solid triangle and dark blue trace = low-angle thrust fault; green = dextral fault; brown = sinistral fault; thin line and yellow trace = low-angle normal fault; solid square and red trace = high-angle normal fault. Rigid plates adjacent to orogen are named following global plate model PB2002 (Bird 2003). Abbreviations of fault and geographic names: ASH = Ashkabad fault; ATF = Altn Tagh fault; CMF = Chaman fault; Deh = Dehshir fault; DF = Dauki fault; EHS = Eastern Himalayan syntaxis; GF = Gawk fault; JF = Jiali fault; K = Kabaw fault; KB = Kuh Banan fault; KLF = Kunlun fault; KSF = Kongur-Shan fault; KXF = Karakax Fault; L = Lakarkuh fault; LCF = Langcang fault; LMS = Longmen Shan; MRF = Main Recent fault; MZT = Main Zagros thrust; NAF = North Anatolia fault; NF = Nayband fault; NTF = North Tabriz fault; QJF = Qujiang fault; QLF = Qinling fault; QLS-NS = Qilian Shan-Nan Shan; RRF = Red River fault; Ta = Tabriz; TFF = Talas-Fergana fault; WCF = West Caspian fault; WKT = Western Kunlun thrust; WSG = Weihe Shanxi graben system and XSH-XJF = Xianshuihe-Xiaojiang fault.

2007; Thatcher 2007), some with continuous shortening and thickening (Houseman & England 1993) and some with deforming blocks (Holt *et al.* 2000; Wang *et al.* 2003; Chen *et al.* 2004). In Iran, continental collision takes place west of 56°E while oceanic plate subducts in the Makran subduction zone to the east. Jackson *et al.* (1995) suggested that Iranian deformation can be described by rigid blocks embedded in deformation belts. The North Anatolia dextral fault zone in eastern Turkey possibly continues to the Main Recent fault in the northern Zagros Mountain (Talebian & Jackson 2002). In Turkey a westward lateral escape of the Anatolia block is seen in GPS measurements (McClusky *et al.* 2000).

Because the orogen is so large, most previous models concern only a part of it (e.g. Iran, Tibet plateau or southeast Asia) (Zhang *et al.* 2004; Chen *et al.* 2004; Vernant *et al.* 2004; Shen *et al.* 2005; Meade 2007; Thatcher 2007). Others made attempts to obtain the entire velocity field of Asia by combining data from geodesy, geological slip rate, with or without constraint from earthquake focal

mechanisms (Holt *et al.* 2000; England & Molnar 2005). For a better estimate of deformation across this plate boundary zone, it is preferable to model Persia–Tibet–Burma as a whole.

Our new kinematic modelling program (NeoKinema) has some strong similarities to methods applied by Holt *et al.* (2000) and England & Molnar (2005) to the same region. In all three studies, geological heave rates and geodetic velocities were merged to estimate regional tectonic flow by a weighted-least-squares method. In all three approaches, geological estimates of fault slip-rates contribute to the target strain-rates of local regions, while uncertainties in geological slip-rates contribute to heterogeneous and anisotropic compliance to the same regions. Differences in the processing of geodetic data, and in the parametrization of the neotectonic velocity field, are details which probably have only minor effects. Distinctions can be made between the treatments of boundary conditions: Holt *et al.* (2000) solved for the Euler poles of surrounding plates as part of their solution (Table 1), while England & Molnar (2005) left

Table 1. Euler poles of (micro)plates with respect to stable Eurasia (EU).

| (Micro)plate | Holt <i>et al.</i> (2000) | England & Molnar (2005) | This study (most models) | This study (final model PTB2007008) |
|---------------------------------|--|--|---|--|
| Amur (AM) | 64.61°N, 158.23°E, 0.077° Ma ⁻¹ (output) | 64.8°N, 156.1°E, 0.060° Ma ⁻¹ (output) | 22.29°N, 286.60°E, 0.091° Ma ⁻¹ (input) 28.06°N, 11.45°E, 0.533° Ma ⁻¹ (input) 24.37°N, 17.65°E, 0.505° Ma ⁻¹ (input) 8.8°N, 284.5°E, 0.181° Ma ⁻¹ (input) | 58.8°N, 157.5°E, 0.034° Ma ⁻¹ (input) 26.22°N, 22.87°E, 0.427° Ma ⁻¹ (input) 28.56°N, 11.62°E, 0.357° Ma ⁻¹ (input) 26.0°N, 279.6°E, 0.128° Ma ⁻¹ (input) |
| Arabia (AR) | | | | |
| India (IN) | 29.78°N, 7.51°E, 0.353° Ma ⁻¹ (output) | | | |
| Sunda (SU) | | | | |
| Tarim | 39.24°N, 98.2°E, −0.539° Ma ⁻¹ (output) | 37.9°N, 97.2°E, −0.49° Ma ⁻¹ (output) | 33.5°N, 99°E, −0.54° Ma ⁻¹ (output, model PTB2006375) | 36.7°N, 97.2°E, −0.45° Ma ⁻¹ (output, model PTB2007008) |
| Yangtze (YA) (‘South China’) | 64.84°N, 156.74°E, 0.12° Ma ⁻¹ (output) | 52.4°N, 159.0°E, 0.075° Ma ⁻¹ (output) | 61.21°N, 142.00°E, 0.206° Ma ⁻¹ (input) | 61.21°N, 142.00°E, 0.206° Ma ⁻¹ (input) |

boundaries free, and our approach is to select and impose boundary velocities (Table 1). In our view, the primary distinctive advantages of NeoKinema are that: (1) geodetic velocities are self-consistently corrected for temporary effects of shallow fault locking before being used to estimate long-term tectonic flow; (2) principal ‘stress directions’ (e.g. seismic moment tensor orientations) are used to constrain orientations and senses of anelastic strain-rate in the continuum between faults; (3) this new constraint permits use of smaller elements (without unpleasant artefacts), and we have taken advantage of this by using $\sim 10 \times$ more elements for better resolution; (4) we obtain the median level of scalar anelastic strain-rate in continuum elements by a bootstrap method instead of assuming it; (5) we search across two tuning parameters to find a best-fit to all data sets (using a method that is independent of finite element size) and (6) we use a local (per-element) post-processing step to obtain *a posteriori* (output) heave rates for all faults, for seismic hazard estimation and other testing.

Our model output can also be used to estimate long-term earthquake rates, based on model fault slip rates and strain rates in deforming continua. We do this with a second program, Long_Term_Seismicity, which utilizes the output of NeoKinema. Previously, Rong (2002) computed three alternate seismicity forecasts for the same region, and used geological and geodetic data (treated separately). The important differences in our approach are that (1) we merge geological with geodetic data instead of using them to make separate forecasts; (2) we use a global calibration of the relation between tectonics and seismicity, rather than a regional one and (3) we forecast seismicity for each small finite element, instead of aggregating it into 21 regions. Our result is a purely tectonic, stationary model of forecast seismicity, which is independent of instrumental or historic earthquake records from this orogen. This makes it possible for us (in principle) to identify any deviations of observed seismicity in the instrumental time period due to release or accumulation of elastic strain.

In this paper, we first obtain long-term velocity and strain rate field by combining geological fault slip rates, geodetic velocities and principal ‘stress directions’ (seismic moment tensor orientations). Then we discuss their implication for deformation in the region. Finally, we estimate long-term earthquake rates (above a given magnitude threshold) and compare them retrospectively with observed earthquake occurrence.

2 METHOD

Here we give a brief description of kinematic finite-element program NeoKinema. A full description of its equations and methods can be

found Appendix S1 (in the Supplementary Material available in the online article). The source code for this program is in Appendix S2 (Supplementary Material).

NeoKinema is a kinematic modelling program, which accepts only velocity boundary conditions, and fits the internal velocity field within the model domain to available data (and/or *a priori* constraints) by a weighted-least-squares method. Unlike dynamic finite element models, NeoKinema does not accept traction boundary conditions or assumed rheologies, or solve the momentum equation. The data sets that NeoKinema can fit include: geodetic velocities (from time/space windows without major earthquakes), geological fault slip rates, principal stress directions (or proxies like seismic moment tensor orientations) and velocity boundary conditions from a plate-tectonic model. NeoKinema outputs long-term-average velocity, long-term-average anelastic strain rate and preferred fault slip rates.

The model domain of NeoKinema is an area within a closed curve on the spherical surface of a non-rotating model Earth. The domain is represented by a 2-D finite element mesh of spherical triangles. Each node in the mesh has two degree-of-freedoms: the southward and eastward components of long-term-average velocity. Differentiation of velocity within each triangle (Kong & Bird 1995) gives the long-term (anelastic) strain rates.

NeoKinema solves for optimal nodal velocities by minimizing a weighted-squares-of-prediction-errors objective function, which includes point constraints (geodetic velocities), slip rate constraints that apply all along a fault trace and other constraints (minimization of strain rates, strain-orientation) that apply over areas of unfaulted continuum. The prediction errors are normalized by the variances of the constraints, respectively, to make them dimensionless. NeoKinema finds a stationary point in a multidimensional velocity-component space with a system of linear equations. Nonlinearities associated with correcting for temporary locking of faults (affecting geodetic velocities) and imposing the strain-rate sense (in unfaulted continuum) are handled by iteration of the solution. Velocity boundary conditions are computed from global models such as PB2002, REVEL (Sella *et al.* 2002), or Global Strain Rate Model (Kreemer *et al.* 2003) and applied around the edges of the models (within the rigid parts of surrounding plates).

Geodetic benchmarks are treated as internal point constraints on the velocity field (with associated uncertainties). Geodetic velocities are ‘corrected’ for temporary locking of faults, using the current model estimates of the fault slip rates, locking depths assigned *a priori* and analytic solutions for rectangular dislocations in a uniform elastic half-space. This requires iteration. If a full covariance matrix for geodetic velocity components is available, we minimize

$(\vec{m} - \vec{g})^T \tilde{N}(\vec{m} - \vec{g})$, where \vec{m} is the vector of model velocity components, \vec{g} is the vector of geodetic velocity components and \tilde{N} is the normal matrix (inverse of the covariance matrix) of the geodetic velocity components.

Faults with positive target heave rates contribute to the target strain rates of all elements they cut through. Uncertainties in fault heave rates (which are allowed to be huge, but not allowed to be zero) contribute to anisotropic compliance of all elements that the faults cut through. The throw rates and throw rate uncertainties of many normal and thrust faults are converted into heave rates and heave rate uncertainties using the assumed fault dips. Dip-slip faults are permitted to slip obliquely (with strike-slip no more than a specified fraction of dip-slip) to allow a more flexible fault network. This is also done by iteration of the solution.

In unfaulted elements an interpolated horizontal principal ‘stress direction’ is used to constrain the horizontal principal directions of the long-term strain rate. Unfaulted elements are assigned zero target strain rates with an assigned uncertainty μ (*a priori*). A larger μ could represent complex or poorly studied areas where unknown faults might be buried and overlooked; however, in this study we have kept μ uniform across the orogen.

As NeoKinema attempts to fit geodetic velocities, geological slip rates and principal stress/strain-rate directions, choices need to be made about relative weights for each type of data. In addition to standard deviation μ associated with the null target rate of continuum strain-rate, there are two ‘tuning’ parameters: (1) length L_0

of fault-trace whose heave-rate constraint gets the same weight as one geodetic velocity and (2) area A_0 of continuum whose stiffness and stress/strain-rate-direction constraints get the same weight as one geodetic velocity. Below, we will describe how we choose these two parameters and the uncertainty μ for the Persia–Tibet–Burma orogen.

3 MODEL CONSTRUCTION

3.1 Input data

Three types of input data are used in the modelling: 366 fault traces with (known or unknown) geological heave rates, 1504 geodetic benchmark velocities and 876 seismic moment tensor orientations (serving as proxies for most-compressive horizontal stress directions).

Fig. 2 shows surface traces and target heave rates for all faults included in our modelling. Active faults and their geological slip rates in central and eastern Asia are from Holt *et al.* (2000), most of which were from the previous compilation by England & Molnar (1997). Where possible, we took heave rates directly from England & Molnar (1997) instead of using slip vectors in Holt *et al.* (2000). For those slip rates that Holt *et al.* (2000) modified or added, we used the slip rate vector to obtain the heave rate components. For shallow-dipping continental-subduction thrust faults (dip $\sim 10^\circ$), the heave rate is approximated by the slip rate. For oblique thrust faults with high

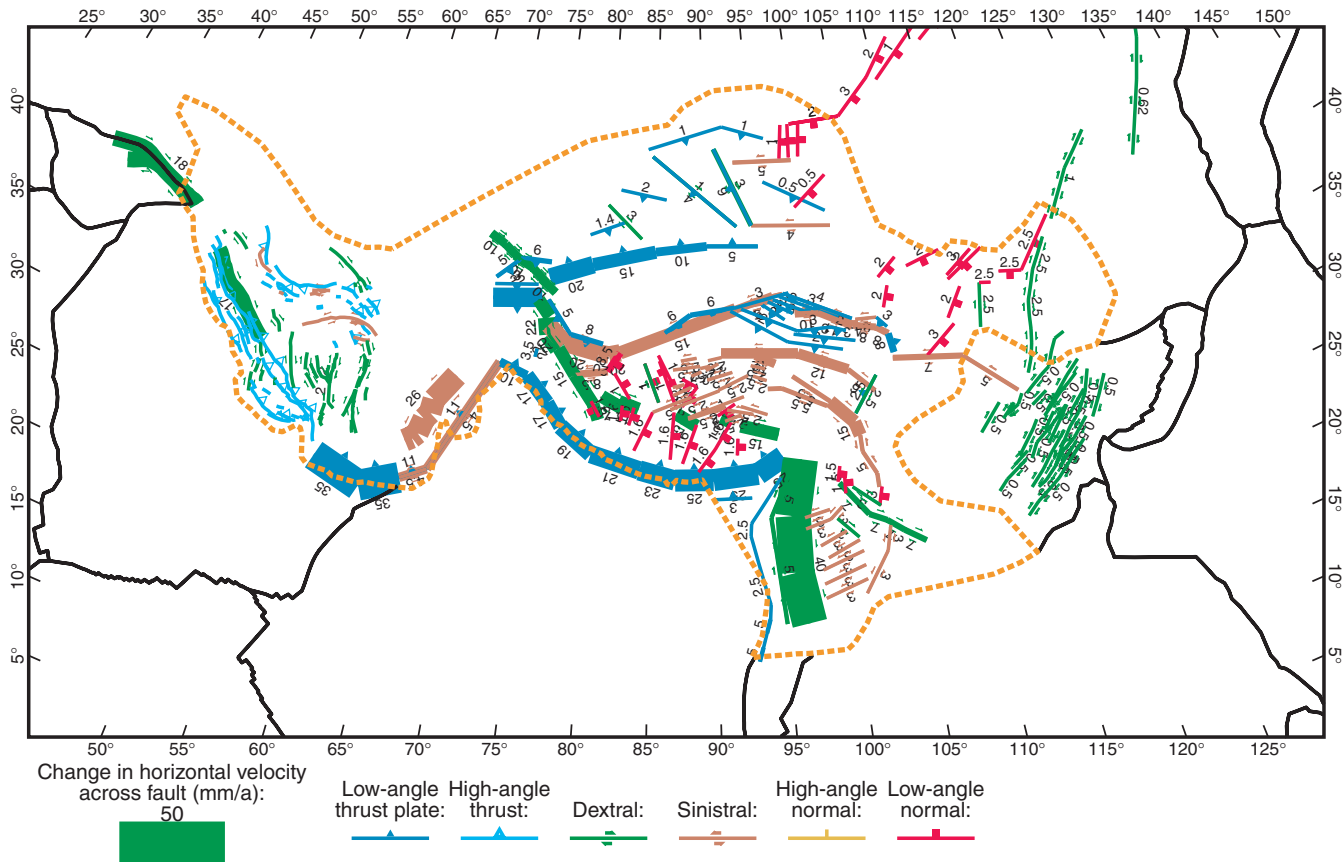


Figure 2. Traces and heave rates (horizontal components of slip rates) of active and potentially active faults in the Persia–Tibet–Burma orogen. Geological slip rates are combined from various sources described in text. Width of coloured bands is proportional to magnitude of heave rate. An uncertainty is assigned to each rate (but not shown in the figure). For faults in Iran that have no available slip rate estimates, a large uncertainty ($\sim 10 \text{ mm a}^{-1}$) is assigned. Many uncertainties are equal to, or greater than, slip rate estimates, which allows these fault to lock or slip backwards.

dip angles such as southwest segment of the IN-EU boundary thrust fault, we decomposed the oblique heave rate vector into convergent and strike-slip components, and input them as separate entries. We assume that each heave rate has a Gaussian distribution with $\pm 2\sigma$ error bounds corresponding to the maximum and minimum heave rates. Then we estimated mean heave rate and its σ from minimum, maximum and best-estimate heave rates. We added the North Anatolia fault (Hubert-Ferrari *et al.* 2002), and digitized major active (or potentially active) faults in Iran (Berberian & Yeats 2001, Fig. 1). Some heave rates are updated; these include: $18 \pm 3.5 \text{ mm a}^{-1}$ on the central and east North Anatolia fault (Hubert-Ferrari *et al.* 2002), $17 \pm 3 \text{ mm a}^{-1}$ on the Main Recent fault (Talebian & Jackson 2002) and $2 \pm 0.2 \text{ mm a}^{-1}$ on the Gowk fault (Walker & Jackson 2002). For those faults in Iran with no heave rate constraints, a large standard deviation $\sim 10 \text{ mm yr}^{-1}$ is assumed. This large uncertainty allows faults to slip in any way permitted by other data in the solution (even with the wrong sense). Therefore, when slip rate is not well constrained, the regional deformation will be determined mainly by the geodetic-velocity, stress/strain-rate-direction and continuum constraints, but will also be influenced by the heterogeneous and anisotropic compliance provided by the faults.

Fig. 3 shows geodetic data used in our modelling. The geodetic data were compiled from various sources. Most data are from the global compilation by Z.K. Shen at UCLA. These data include the compilation of Kreemer *et al.* (2003), which collected data from various published sources up to 2001 and put velocities into one best fit self-consistent NNR reference frame, plus a GPS solution from the Crustal Motion Observation Network of China (Wang *et al.* 2003). We added some recent solutions in China (Wang *et al.* 2001) and Iran (Tatar *et al.* 2002; Vernant *et al.* 2004). Recent data from Chen *et al.* (2004) in central Tibet is an updated subset of Wang *et al.*

(2001); since RMS misfit between these two solutions at collocated sites is small ($\sim 1 \text{ mm yr}^{-1}$), we choose not to include velocities from Chen *et al.* (2004) in our model. Except for the geodetic data from Kreemer *et al.* (2003), all are in the Eurasia reference frame. We convert data from Kreemer *et al.* (2003) from NNR to Eurasia frame by using a EU-NNR pole (56.3°N , -98.6°E , $0.273^\circ \text{ Myr}^{-1}$) in Kreemer & Holt (2001).

Slight variations in the definition of the EU reference frame may exist among various published sources because different groups used different stations to tie to the global reference frame and define stable Eurasia. A common approach adopted by most previous studies is assuming a rigid rotation exists for each study such that they can be rotated into one self-consistent reference frame (Holt *et al.* 2000; Kreemer *et al.* 2003; England & Molnar 2005). We find that rigid-body rotation does not necessarily lead to reduced post-fit residuals at collocated sites. Instead, we accept the slight variations of EU definition in respective GPS solutions. All GPS solutions used in this study have RMS misfits (with one another) of 2.9 mm a^{-1} or less, compatible with $1-\sigma$ uncertainties of all data ($2.23 \pm 1.15 \text{ mm yr}^{-1}$). So we expect that our model will be able to represent relative velocities above the level of $\sim 2.9 \text{ mm a}^{-1}$. To allow for possible slight differences between the EU reference frame of our boundary conditions and the EU reference frame of the geodetic studies, we utilized the option within NeoKinema which treats the reference frame of the input data as free-floating. Under this option, the program augments the covariance matrix of the geodetic velocity components with three very large eigenvalues corresponding to rotations of the whole geodetic network about three perpendicular Earth-centred axes. When the covariance matrix is inverted to create the normal matrix, these lead to three very small eigenvalues associated with the same rotations. Then, the objective function of NeoKinema

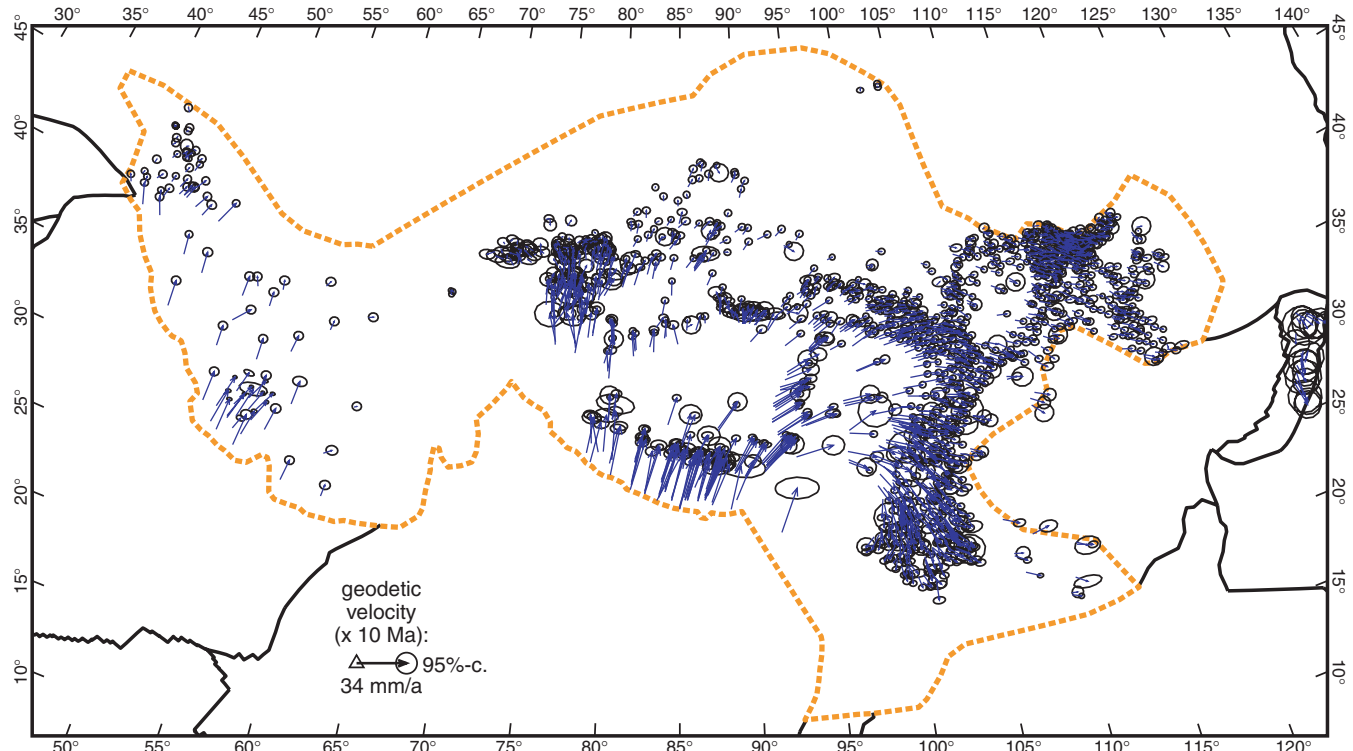


Figure 3. Relative horizontal velocities of geodetic benchmarks in the Persia–Tibet–Burma orogen. Geodetic data are compiled from various sources listed in text. All geodetic benchmark velocities are in the Eurasia reference frame. Plotted velocity vectors are projected displacements during 10 million years. Ellipses show 95 per cent confidence limits.

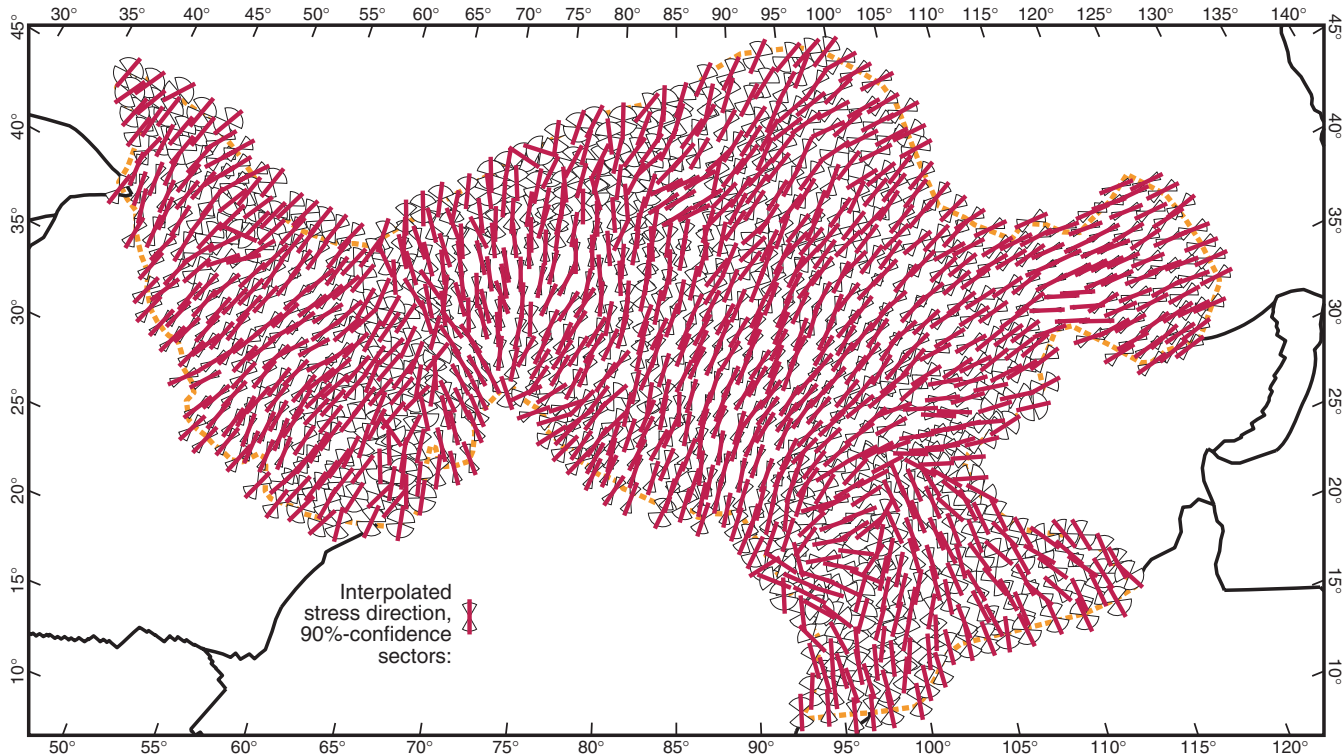


Figure 4. Interpolated most-compressive horizontal principal ‘stress directions’ shown by thick red lines. 90 per cent confidence limits surrounding each ‘stress direction’ are also shown with white fans. Data from 2003 release of the World Stress Map consists primarily of trends of most-compressive principal axes of seismic moment tensors. An interpolation method developed by Bird & Li (1996) was used to interpolate the stress/strain-rate directions over the whole model domain. To increase legibility, only 1/3 of interpolated directions are shown in this figure, but all of them were used in the NeoKinema simulation.

becomes insensitive to the difference (if any) between the reference frame used for benchmark velocities and the reference frame used for velocity boundary conditions. Further details may be found in Appendices S1 and S2.

Interseismic geodetic velocities at benchmarks adjacent to faults are subject to elastic fault-locking effects. Since long-term velocity in our model is on the timescale of $\sim 10^4$ to 10^6 yr, averaging over several seismic cycles, program NeoKinema applies elastic-dislocation-patch corrections to geodetic velocity data (Liu & Bird 2002; Appendices S1 and S2). We assume that the minimum/maximum locking depths are 14/40 km in subduction zones and 1/11 km in all other faults. For comparison, the recent elastic microplate model which Meade (2007) fit to geodetic data in the Tibet region implied an optimal lower locking depth (outside subduction zones) of 17 km; however, this value was not sharply resolved, and his increase in χ^2 at our preferred lower locking depth of 11 km was only 5 per cent over the minimum he obtained.

Significant earthquakes during the time window of geodetic data collection may introduce coseismic and postseismic effects into geodetic data. It is difficult to determine which stations might be subject to such effects without looking at raw GPS position time series. We assume published interseismic velocities used here have removed such anomalous data, as elaborated by Kreemer *et al.* (2003).

‘Stress-direction’ data are from the World Stress Map 2003 (Reinecker *et al.* 2003). In this region, most are actually strain-rate-direction data obtained from the trends of most-compressive principal axes of seismic moment tensors. Two justifications can be offered for using moment tensor orientations (which are technically strain-rate orientations) as proxies for stress directions: (1) There is evidence for general (regional) parallelism of these two

fields (Molnar *et al.* 1973; England & Molnar 2005) and (2) After interpolation, we actually use these directions to constrain model strain-rate directions anyway. These data are interpolated by program NeoKinema to each element centre using the nonparametric interpolation method of Bird & Li (1996). The essential idea of this method is that empirical (non-parametric) distributions of angular discrepancies between present stress directions (as a function of distance between them) provide a basis for non-parametric statistical estimation of the distribution of stress directions at any desired interpolation point. Specifically, NeoKinema uses the variant method in which data are geographically pre-clustered (achieving an effect similar to that of the kriging method for scalar data), not the variant method in which they are all assumed to be mutually independent. Fig. 4 shows the interpolated ‘stress directions.’ In continuum elements without active faults, we assume most-compressive horizontal principal strain rate axes should align with interpolated $\hat{\sigma}_{1h}$.

3.2 Boundary conditions

Table 1 includes Euler poles for the surrounding rigid plates that we used to compute velocity boundary conditions for all edges of our grid. We use the Eurasia velocity reference frame. Since Euler poles in updated global plate model PB2002 are in the Pacific reference frame, we converted them into the Eurasia-fixed reference frame by adding the PA-EU relative rotation from PB2002 (which was taken from NUVEL1-A). For most models (i.e. PTB2006001-PTB2006448), Euler poles and rotation rates from PB2002 were used to compute relative motion between rigid plates Anatolia (AN), Arabia (AR), India (IN), Burma (BU), Yangtze (YA), Amur (AM) and Eurasia (EU). In these models, the relative motion between

Sunda plate (SU) and Eurasia was computed using pole and rotation rate (8.8°N , 75.5°W , $0.181^\circ\text{ Ma}^{-1}$) from Sella *et al.* (2002). We did not use the SU-EU pole reported by Rangin *et al.* (1999) and Chamot-Rooke & Le Pichon (1999), which incorrectly predicts northeastward motion in the southeastern part of the orogen (South China Sea or north Sunda block), inconsistent with east to south-eastward motion in the GEODYSEA study, and in Chinese studies.

Recent studies (Sella *et al.* 2002; Kreemer *et al.* 2003; McClusky *et al.* 2003; Socquet *et al.* 2006) suggest a slower motion of Arabia and Indian Plates relative to Eurasia, compared to the predictions from NUVEL1-A that were used in PB2002. Predicted velocities from these studies at the boundary nodes within rigid Arabia or Indian Plates orient at roughly the same direction but slightly differ in magnitude. There is some controversy about the motion of the Amur Plate relative to Eurasia. For example, PB2002 predicts $\sim 8\text{--}9\text{ mm yr}^{-1}$ in largely eastward orientation (azimuth $\sim 89^\circ$ to $\sim 109^\circ$) at the boundary nodes in Amur Plate. REVEL (Sella *et al.* 2002) predicts $\sim 6\text{--}7\text{ mm yr}^{-1}$ with azimuth from $\sim 145^\circ$ to 170° in SSE direction. On the contrary, the Global Strain Rate Model (GSRM) (Kreemer *et al.* 2003) predicts much smaller magnitude $\sim 2\text{ mm yr}^{-1}$ with azimuth from $\sim 119^\circ$ to $\sim 145^\circ$. In models PTB2007001–PTB2007009 we explored the effects of these different motion between rigid plates Arabia, Indian, Amur, Sunda and Eurasia, using pole and rate estimates from Sella *et al.* (2002) and Kreemer *et al.* (2003) as representative examples. In all models computed velocity boundary conditions were imposed at boundary nodes, which are believed to lie within the rigid parts of these plates.

4 MODELLING AND RESULTS

There are three primary adjustable ('tuning') parameters in our kinematic modelling: strain rate uncertainty allowance μ , reference length L_0 and reference area A_0 .

μ is the *a priori* uncertainty of continuum deformation rate, the deviation of background anelastic strain-rate from nominally zero strain-rate in unfaulted crust. Unlike previous studies that typically assumed values analogous to μ (e.g. Holt *et al.* 2000; England & Molnar 2005), we use a bootstrap method involving a systematic search to find its optimal value.

Dimensional parameters L_0 (in m) and A_0 (in m^2) determine the relative weights of fault-trace-based heave-rate data and of area-based continuum-stiffness and strain-orientation constraints, respectively, relative to point-based geodetic data. There is a trade-off between fitting fault heave-rates, geodesy, continuum stiffness and stress/strain-rate-orientations. For fixed L_0 , increasing A_0 put relatively less weight on continuum stiffness and stress/strain-rate-orientations and more weight on geodesy and fault slip rates. Therefore, the fit to geodetic and slip rate data improves but the fit to continuum and stress/strain-rate-directions degrades. For fixed A_0 , increasing L_0 reduces the relative weight on fault heave rates and increases the relative weights on geodetic, continuum and stress/strain-orientations. Consequently misfit errors of geodetic data, continuum stiffness and stress/strain-rate-directions are reduced but misfit error of fault heave rates is increased. Increasing both L_0 and A_0 in proportion increases the relative weight on geodetic data, etc.

We performed a systematic grid search in parameter space. In models PTB2006001 to PTB2006448, six μ values were tested, from 2.00×10^{-17} to $1.28 \times 10^{-15}\text{ s}^{-1}$. We experimented with eight L_0 values from 1.0×10^3 to $1.28 \times 10^5\text{ m}$. We also explored eight A_0 values from 2.0×10^6 to $4.38 \times 10^9\text{ m}^2$. For each μ , we calculated

misfit errors for 64 combinations of L_0 and A_0 , respectively. For each model both the L1-norm (mean absolute value of non-dimensional prediction errors, which are dimensional prediction errors each divided by the corresponding prior/input datum standard deviation) and L2-norm (RMS value of non-dimensional prediction errors) are calculated for continuum-stiffness, fault-heave-rate, geodetic-velocity and stress/strain-rate-direction data, respectively. We also conducted tests with larger geodetic uncertainties (intended to reflect reference-frame issues) and alternative velocity boundary conditions for Indian, Arabia, Amur and Sunda Plates based on Euler poles and rotation rates from Sella *et al.* (2002) and Kreemer *et al.* (2003). A total of 457 models were computed. Appendix S3 (Supplementary Material) lists all the models with L0, L1 and L2-norms for each data class.

Large μ tends to reduce misfit errors of fault, geodesy and stress/strain-rate-direction data, because of the increased flexibility of the F-E grid added by large μ in each element. However, another consideration is that the *a priori* μ should be consistent with the *a posteriori* continuum strain-rates of relatively successful models, suggesting a bootstrap method for determining μ . Fig. 5 shows L2-norm errors for different values of μ , and also the continuum strain-rates that were obtained in these calculations. The mean and RMS values of continuum strain-rate tend to increase slightly with increasing μ , but are not proportional to it. Each μ is shown along with corresponding mean absolute value and RMS value of continuum strain rate for different (L_0, A_0) combinations. The mean absolute and RMS value represent lower and upper bounds on the expected continuum strain rate; a proper μ should be compatible with these bounds for a range of L_0 and A_0 . $\mu = 4.00 \times 10^{-16}\text{ s}^{-1}$ meets this criterion.

Continuum strain-rate is apparently strongly determined by many factors other than the μ assumed *a priori*. These intrinsic causes of continuum deformation include fault incompatibilities at triple junctions, fault discontinuities, discrepancies between adjacent fault slip rates, undiscovered faults and omitted minor faults. In our current model we include only major faults. However, large numbers of unmapped faults may also exist in the orogen. For example, Taylor *et al.* (2003) discovered pervasive closely spaced conjugate strike-slip faults in central Tibet. Pollastro *et al.* (1998) mapped numerous small faults across Iran in addition to major ones. These unknown, unmapped and/or unmodelled faults contribute to the relatively high continuum strain rate.

Given μ , we explored (L_0, A_0) space for the optimal L_0 and A_0 . Fig. 6 shows the RMS normalized misfit errors versus L_0 at different values of A_0 . Fig. 7 shows the L2 misfit errors versus A_0 at different values of L_0 . In Figs 6 and 7 we also highlight the ranges of L_0 and A_0 which we consider 'preferred' for this problem. The fit to continuum-stiffness and principal 'stress directions' is less sensitive to the lower range of A_0 from 2×10^6 to $1.62 \times 10^8\text{ m}^2$ at any L_0 but the fit to geodetic data and fault slip rate improves for A_0 larger than $1.62 \times 10^8\text{ m}^2$. When L_0 is larger than $3.2 \times 10^4\text{ m}$, the fit to continuum, 'stress directions,' and geodetic data does not improve much, but the fit to geological heave rates degrades. So L_0 cannot be too large. We found that in models PTB2006001–PTB2006384, PTB2006375 with (L_0, A_0) of $(6.4 \times 10^4\text{ m}, 1.46 \times 10^9\text{ m}^2)$ and μ at $4.0 \times 10^{-16}\text{ s}^{-1}$ fits all data within their uncertainty levels: geological heave rates, geodetic velocities and interpolated 'stress directions' were fit with RMS normalized misfit errors of 1.06, 1.69 and 0.72 standard deviations, respectively. We also tested imposing a uniform 2.1 mm yr^{-1} as the uncertainty in both the East and South components of geodetic velocities in model 385–448 (Appendix S3, online Supplementary Material), which brings RMS misfit to

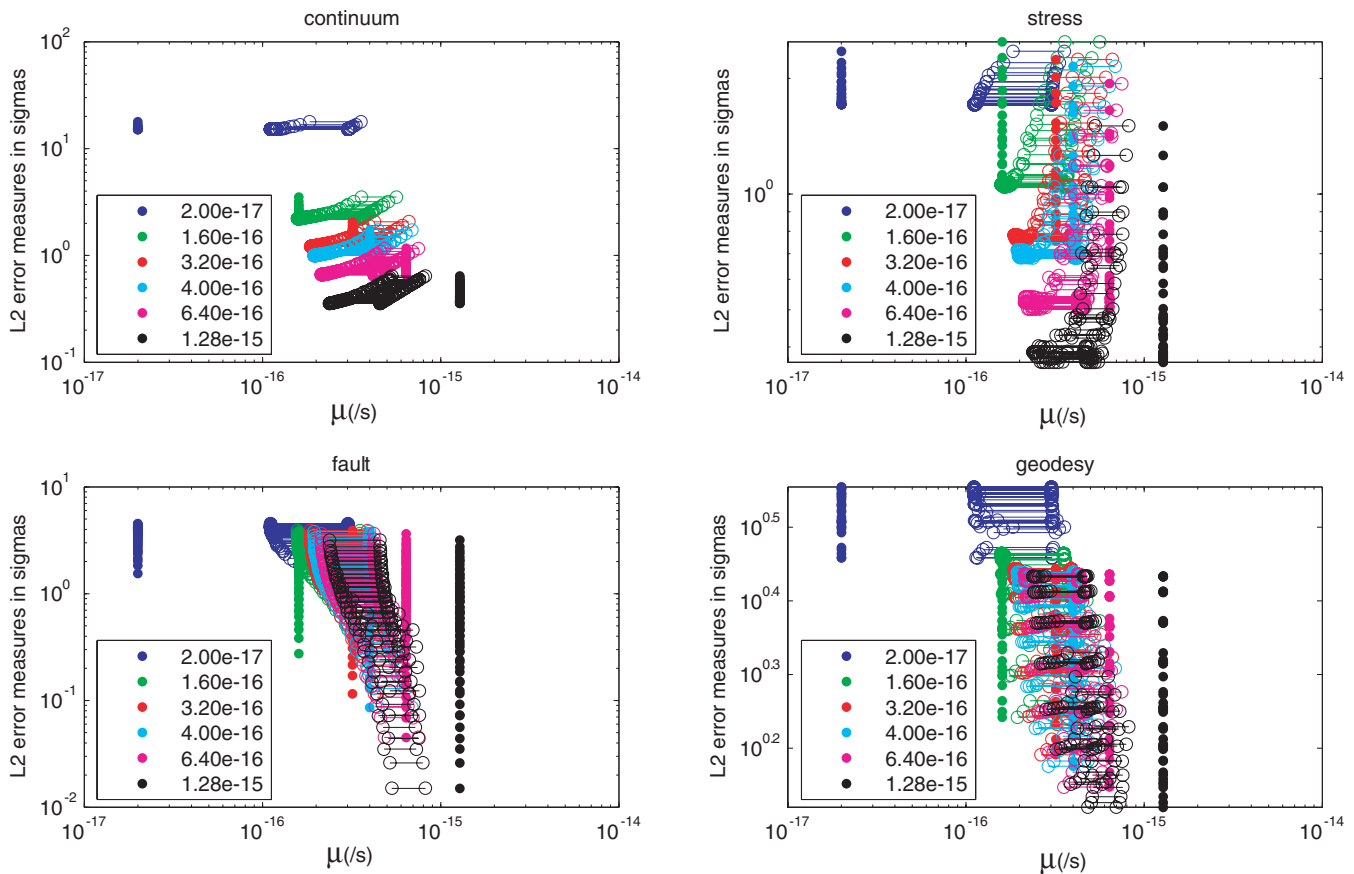


Figure 5. L2-norm errors (RMS prediction errors in units of standard deviations) of continuum-stiffness, stress/strain-rate-direction, heave-rate and geodetic-velocity versus different μ values assumed *a priori*. For each μ , L2 misfit errors of 64 models with various L_0 and A_0 are shown as filled dots. L2 misfit errors of these models versus the mean absolute value and RMS value of continuum deformation rate associated with each μ are also shown as open circles connected by horizontal lines. Different μ and associated continuum deformation rate are represented by different colours. For self-consistency, μ should fall within the limits of the mean absolute value and RMS value of continuum deformation rate. $\mu = 4.0 \times 10^{-16} \text{ s}^{-1}$ meets this criterion.

$\sim 3.1 \text{ mm a}^{-1}$, comparable to the differences between the various GPS studies. Increasing uncertainty reduces normalized misfit errors of geodetic data, but the deformation patterns and rates remain largely unchanged.

In models PTB2007001–PTB2007009, we explored the effects due to the slower movement between plates Arabia and Indian relative to Eurasia, and different relative motion between plates Amur, Sunda and Eurasia. As discussed in boundary condition section, we used Euler poles and rotation rates for these plates from Sella *et al.* (2002) and Kreemer *et al.* (2003). The slower convergence between Arabia, Indian Plates with regard to Eurasia reduces the preferred μ from 4.0×10^{-16} to $3.7 \times 10^{-16} \text{ s}^{-1}$. As a result, the new preferred model is PTB2007008, which assigns AR-EU and IN-EU motion based on Sella *et al.* (2002) and AM-EU and SU-EU motion based on Kreemer *et al.* (2003). With (L_0, A_0) of $(6.4 \times 10^4 \text{ m}, 1.46 \times 10^9 \text{ m}^2)$ and μ at $3.7 \times 10^{-16} \text{ s}^{-1}$ the model fits all data within their uncertainty levels, comparable to PTB2006375. The RMS normalized misfit errors for geological heave rates, geodetic velocities and interpolated ‘stress directions’ are $1.077, 1.683$ and 0.722 standard deviations, respectively. The corresponding RMS misfit error for geodesy is $2.85 \pm 1.96 \text{ mm a}^{-1}$, comparable to the geodetic data uncertainty level of $2.23 \pm 1.15 \text{ mm yr}^{-1}$ as well as the RMS discrepancy ($\sim 2.9 \text{ mm yr}^{-1}$) among collocated geodetic measurements. The RMS error of principal ‘stress directions’ is $\sim 11.8^\circ \pm 3.5^\circ$, and the model gives comparable RMS normalized misfit errors for

continuum and fault slip rate. Note that from PTB2007007 to PTB2007009, using the AM-EU pole of Kreemer *et al.* (2003) improves the fit to data. However, using different SU-EU poles from either Sella *et al.* (2002) or Kreemer *et al.* (2003) does not make much difference in data fitting and the resulting deformation pattern as shown in PTB2007008 and PTB2007009.

Preferred model PTB2007008 has strain rate uncertainty μ at $3.7 \times 10^{-16} \text{ s}^{-1}$. For typical element dimension of $\sim 100 \text{ km}$, this strain rate uncertainty would imply a relative velocity uncertainty of $\sim 1.2 \text{ mm a}^{-1}$. The value $3.7 \times 10^{-16} \text{ s}^{-1}$ can also be expressed as 1.2 per cent Ma^{-1} , suggesting that over the duration of the India–Asia collision, most crustal blocks have not retained their original shapes.

Fig. 8 shows the predicted long-term-average velocity field in the Persia–Tibet–Burma orogen from preferred model PTB2007008. It predicts major tectonic features in the region, such as distributed deformation across the Zagros fold-and-thrust belt in Iran, the Tibet plateau and the Indo-Burma ranges of southeast Asia. West of 60°E , most convergence between the Arabia and Eurasia Plates is accommodated across the Zagros fold-and-thrust belt. In eastern Iran (from $\sim 60^\circ\text{E}$ to 65°E) AR-EU plate motion is mainly taken up by the Makran subduction zone. The Tibetan plateau undergoes significant N–S contraction and E–W extension ($\sim 20 \text{ mm a}^{-1}$) involving westward motion of the northwest Himalaya and eastward extrusion of southeast Tibet. East of $\sim 80^\circ\text{E}$ crust in the interior of Tibet flows

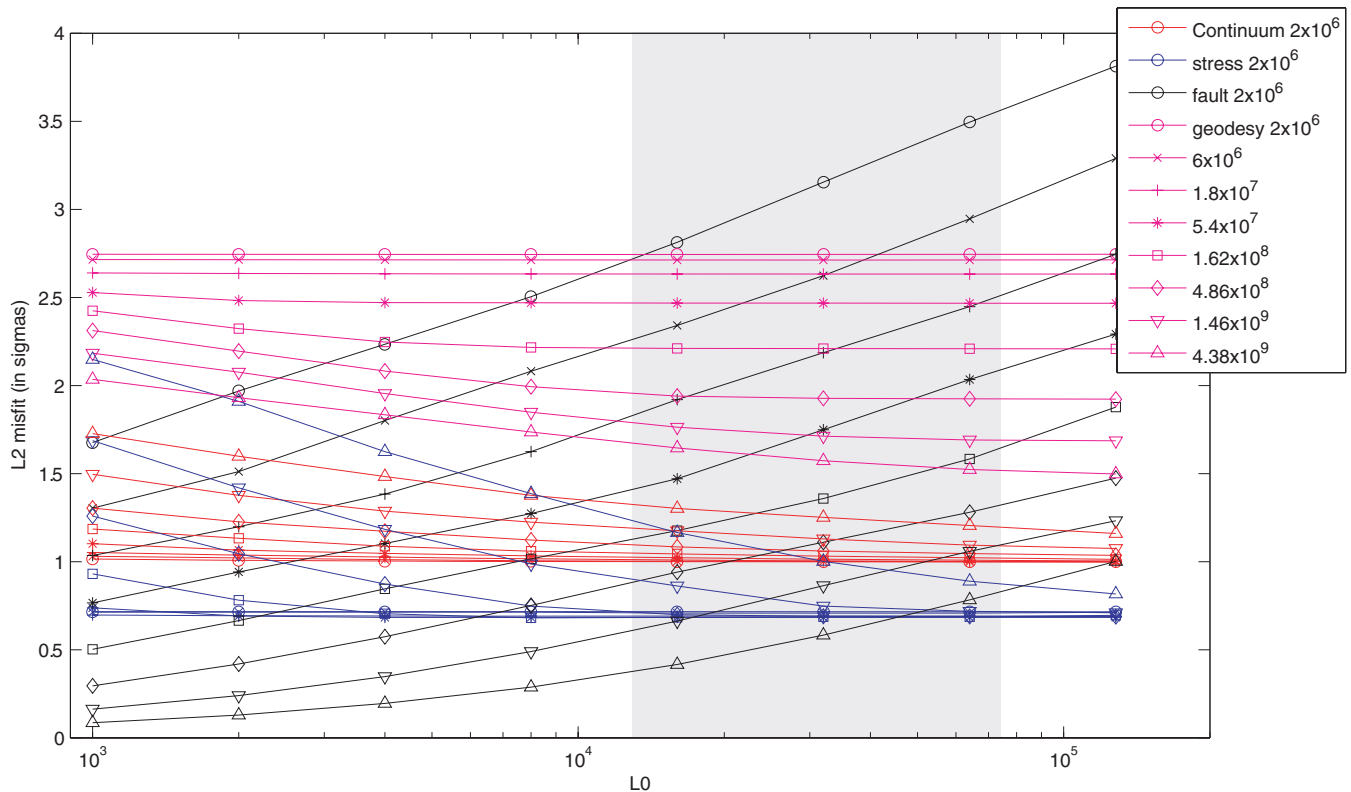


Figure 6. L2-norm misfit errors (dimensionless, linear scale) versus reference length L_0 in metres, on a logarithm scale. Continuum (strain-rate), stress (direction), fault (heave-rate) and geodetic (velocity) errors are represented by symbols and lines in red, blue, black and magenta, respectively. Different symbols (circle, cross, plus, star, rectangle, diamond, inverted triangle and upright triangle) represent misfit errors versus L_0 at different A_0 ($= 2 \times 10^6, 6 \times 10^6, 1.8 \times 10^7, 5.4 \times 10^7, 1.62 \times 10^8, 4.86 \times 10^8, 1.46 \times 10^9$ and 4.38×10^9 m 2). Grey bar indicates range of L_0 (1.6×10^4 – 6.4×10^4 m) where preferred values are located.

northeastward due to N–S contraction and rotates clockwise around the Himalaya syntaxis into its southeastern borderland. Significant transpressive deformation exists along both the western and eastern segments of the IN–EU plate boundary zone. Across the Kunlun, Xianshuihe–Xiaojiang and Longmen Shan faults distributed deformation grades into slower deformation to the east in the south China block, which moves southeastward at rates of 8–10 mm a $^{-1}$. The central Iran and Lut blocks, south Caspian basin, Helmand block, Tarim basin, Gobi–Alashan and Ordos blocks have relatively coherent motion with little internal deformation. The velocity gradients between these relatively rigid blocks and surrounding distributed deformation zone are absorbed by known faults.

Fig. 9 shows the common logarithm of the magnitude of the principal strain rate (including faulting) whose magnitude is greatest, in colours, which are overlain by icons representing the anelastic strain-rate tensors. The semi-rigid blocks (e.g. central Iran, southern Caspian basin, Tarim basin, Gobi–Alashan platform, Qaidam basin, Ordos block and Dzungar basin) identified in the velocity field can be more readily recognized in this strain-rate plot. They have lower strain rates of 10^{-17} – 10^{-16} s $^{-1}$ compared to 10^{-15} – 10^{-14} s $^{-1}$ in surrounding fast-deformation zones. Slight differences in internal strain rate exist among these blocks, suggesting spatially heterogeneous strength. The deformation style in the interior of Tibet is mainly strike-slip and normal faulting with principal axes of N–S compression and E–W extension, consistent with earthquake focal mechanisms. Overall, a mixture of distributed deformation and active faulting describes the deformation pattern in Tibet, western segments of the IN–EU boundary zone (near the Chaman fault) and

eastern segments (Indo–Burma ranges and Saging fault) which are characterized by transpressive deformation. Notably, a deforming transition zone between the IN–EU subduction east of 70°E and the Helmand block also extends further north to the west of the Pamirs. This northward extension of the deforming zone is characterized by strike-slip faulting. Even though there are no geodetic or heave-rate data in the region (Figs 2 and 3), our model predicts its general features, and they correspond well with earthquake occurrence in the global CMT catalogue. The Turan shield north of the Helmand block shows ENE–WSW-trending thrusting with strain rate $\sim 3 \times 10^{-16}$ s $^{-1}$. There is one thrust event (1984.03.19 $m = 6.99$, 40.59°N, 63.24°E) with focal mechanism that is consistent with local tectonic compression. The NNW–SSE compression is probably caused by northward indentation by the rigid Helmand block. In Iran, relative convergence between the Arabia and Eurasia Plates is accommodated by distributed deformation in the Zagros fold-and-thrust belt and in the Alborz and Kopet Dagh to the north. There is significant shearing along the eastern boundary of the Lut block. Our long-term strain-rate map shows that the deformation in Persia–Tibet–Burma is a mixture of semi-rigid block and distributed deformation.

Table 2 lists and Fig. 10 displays posterior (output) long-term-average fault heave rates from model PTB2007008. It is important to understand that fault offset rates are both input to NeoKinema and output from NeoKinema. The *prior* or ‘input’ values always include a positive standard deviation, which is allowed to be arbitrarily large. The *posterior* or ‘output’ values obtained from post-processing of the preferred converged solution have no uncertainties, but instead

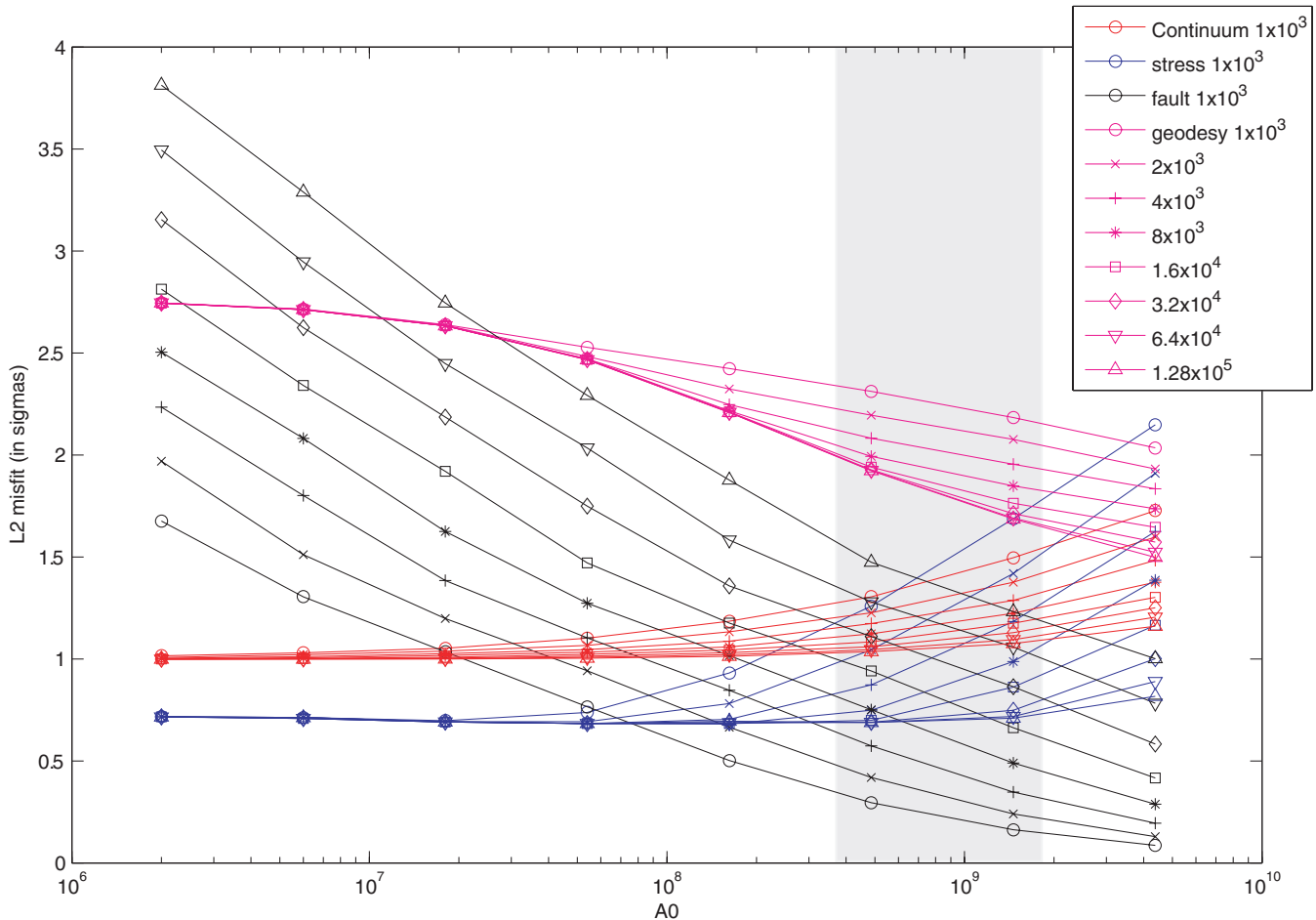


Figure 7. L_2 -norm misfit errors (dimensionless, linear scale) versus reference area A_0 in m^2 , on a logarithmic scale. Colour convention is same as in Fig. 6. However different symbols (circle, cross, plus, star, rectangle, diamond, inverted triangle and upright triangle) represent misfit errors versus A_0 at different $L_0 (= 1 \times 10^3, 2 \times 10^3, 4 \times 10^3, 8 \times 10^3, 1.6 \times 10^4, 3.2 \times 10^4, 6.4 \times 10^4$ and 1.28×10^5 m). Grey bar indicates range of A_0 where preferred values are located.

are best-estimate model predictions obtained by balancing all available constraints. Fig. 11 shows a comparison of input geological heave rates (with uncertainty ranges) to output heave rates. There are a few cases in which the output does not lie within two (input) standard deviations of the prior or input value (northern segment of Sagaing fault, three segments of Himalaya front, Chaman fault, part of the western IN-EU boundary, Arab front, one segment of the Kunlun fault, part of the Pamir thrust belt and south Tien-shan). However, more than 95 per cent of output offset rates lie within two input standard deviations of their corresponding input values.

The Sagaing fault had an input geological slip rate of 40 ± 10 $mm\ a^{-1}$ (prior estimate \pm two prior standard deviation) while the corresponding output best-estimates in our preferred model are $22\ mm\ a^{-1}$ in the northern segment, $34\ mm\ a^{-1}$ in the central segment and $35\ mm\ a^{-1}$ in the southern segment. Three segments of the Himalaya front thrust at $\sim 85^\circ E$ and east had input closing/convergence rates of 23 ± 7 , 25 ± 10 and $25 \pm 10\ mm\ a^{-1}$ while corresponding output best-estimates in our preferred model are ~ 12 and ~ 14 and $\sim 14.5\ mm\ a^{-1}$, close to the low ends of geological slip-rate estimates.

The Chaman fault and western IN-EU boundary ($65-72^\circ E$) accommodate motion between the India Plate and the Helmand block. The input sinistral rate on the Chaman fault was $26 \pm 10\ mm\ a^{-1}$ resulting in output rates of $2-22\ mm\ a^{-1}$ (varying along strike). The

southwest end of the western IN-EU boundary ($65-67^\circ E$) had an input closing (horizontal convergence) rate of $4.5 \pm 3\ mm\ a^{-1}$ and a corresponding output rate of $10\ mm\ a^{-1}$. This apparent underestimate of Chaman slip rate and overestimate of horizontal convergence rate on the southwest segment of the IN-EU boundary probably resulted from a trade-off between these two faults, which both accommodate transpressive deformation. The lack of geodetic data and stress/strain-rate-direction data (Fig. 12) combine with a possibly inadequate representation of local fault traces to prevent the model from better resolving slip rates on these faults.

In the Pamirs and south Tien-shan, thrust faults at $70-75^\circ E$ had input closing/convergence rates of $22 \pm 6\ mm\ a^{-1}$ resulting in corresponding output rates of $10\ mm\ a^{-1}$. The central segment of a dextral strike-slip fault west of the West Kunlun thrust had an input dextral rate of $22 \pm 10\ mm\ a^{-1}$ with a corresponding output rate of $7\ mm\ a^{-1}$. Both of these output rates are smaller than the corresponding inputs. Considering that the slip rates of nearby faults such as the Talas-Fergana fault, Tien-shan fault, Altyn Tagh fault, Karakax fault and Karakorum fault are all consistently estimated (in model output) to be near the lower ends of their input slip rate ranges, we interpret that these input geological slip rates of $12-32\ mm\ a^{-1}$ might have been overestimated by previous authors.

There has been a debate about whether tectonic deformation in Tibet can be better described by ‘block-like’ models (Avouac &

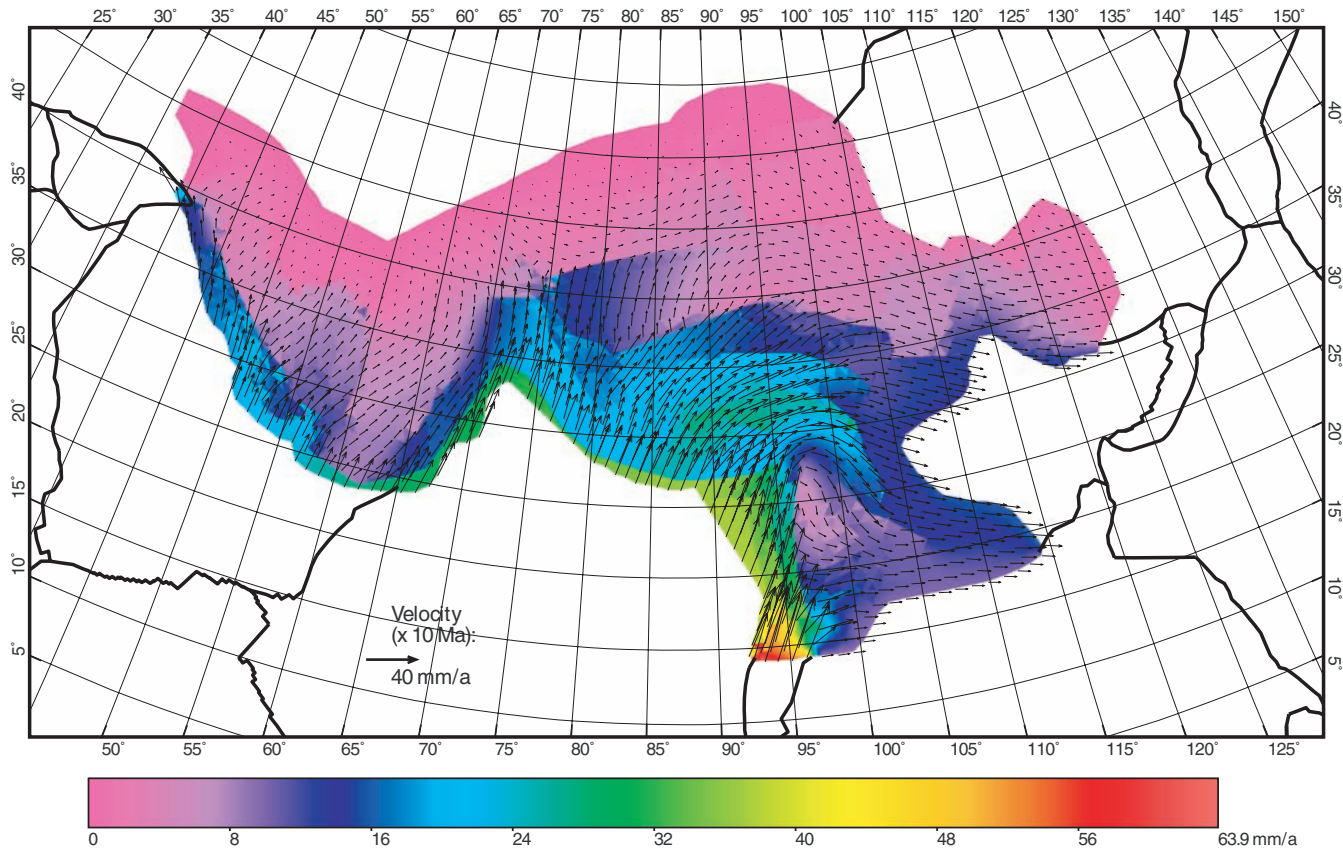


Figure 8. Long-term-average velocity field of preferred model PTB2007008. Colour map represents velocity magnitude (relative to stable Eurasia). Velocity vectors are indicated by thin arrows. Thick lines represent major plate boundaries in PB2002.

Tapponnier 1993; Peltzer & Saucier 1996) or distributed/continuous-shortening-and-thickening models (Houseman & England 1993). In block-like models, the IN-EU collision zone is composed of lithospheric blocks and deformation mainly takes place along block boundaries delineated by long, rapidly slipping strike-slip faults. N–S shortening of Tibet is accommodated by rapid eastward extrusion between major strike-slip faults bounding the region, giving slip rates $\sim 20\text{--}30 \text{ mm a}^{-1}$ on these strike-slip faults. In distributed-shortening-and-thickening models, the crust undergoes continuous shortening and thickening with less eastward extrusion of Tibet at a rate $<10 \text{ mm a}^{-1}$ (Houseman & England 1993). The slip rates on long strike-slip faults such as the Altyn Tagh and Karakorum have been the focus of this debate. Different models are preferred by different groups partly because geodetic and geological slip rates do not agree. England & Molnar (1997) suggested that high slip rates ($20\text{--}30 \text{ mm a}^{-1}$) on the Altyn Tagh, Karakorum and Karakax fault are inconsistent with the strain pattern of the rest of the region.

In this study, the NW-striking, ~ 700 -km-long right-lateral Karakorum fault was assigned a wide input range ($14.5 \pm 12.5 \text{ mm a}^{-1}$) due to ambiguous estimates from geological observations, which range from $32 \pm 8 \text{ mm a}^{-1}$ (Avouac & Tapponnier 1993) to $4\text{--}8 \text{ mm a}^{-1}$ (Murphy *et al.* 2000; Brown *et al.* 2002). The best-estimate output slip rate from our preferred model is $4\text{--}5 \text{ mm a}^{-1}$ (varying along strike), which is towards the lower end of the input slip rate range. It is much smaller than the geological inference ($32 \pm 8 \text{ mm a}^{-1}$) by Avouac & Tapponnier (1993) but agrees with a geological estimate of $\sim 6 \text{ mm a}^{-1}$ for the southern Karakorum

fault since 11 Ma (Murphy *et al.* 2000). It is also consistent with the maximum of 7 mm a^{-1} inferred from InSAR observations (Wright *et al.* 2004) and with interpretations of geodetic measurements, which suggest $11 \pm 4 \text{ mm yr}^{-1}$ (Banerjee & Burgmann 2002) to $3 \pm 5 \text{ mm a}^{-1}$ (Jade *et al.* 2004).

Our preferred model gives an output value of $\sim 13 \text{ mm a}^{-1}$ sinistral slip along the central Altyn Tagh fault, less than ‘block-like’ models predict ($20\text{--}30 \text{ mm a}^{-1}$) (Avouac & Tapponnier 1993; Peltzer & Saucier 1996). However it agrees with a geodetically determined rate of $9 \pm 5 \text{ mm a}^{-1}$ (Bendick *et al.* 2000) and a Holocene slip rate of $17 \pm 3 \text{ mm a}^{-1}$ (Peltzer *et al.* 2006).

Our model gives output slip rates of $4\text{--}8 \text{ mm a}^{-1}$ along the Karakax fault, agreeing with a geodetic estimate of $7 \pm 3 \text{ mm a}^{-1}$ (Shen *et al.* 2001) as well as the lower end of the input range of $19.9 \pm 19.9 \text{ mm a}^{-1}$.

Our preferred model’s output slip rates on the Tien Shan fault increase progressively westward from $\sim 3 \text{ mm a}^{-1}$ at 92°E to $\sim 14 \text{ mm a}^{-1}$ at 77°E , consistent with geodetic measurements (Shen *et al.* 2001). The output long-term-average rate is $6\text{--}12 \text{ mm a}^{-1}$ on the Kunlun fault and 2.2 mm a^{-1} on the Longmenshan fault. The model shortening rate across the northeastern margin of the Tibetan Plateau is $\sim 10 \text{ mm a}^{-1}$. It should be noted that these rates also agree with rates from a more recent geodetic study that we did not include in the inversion (Zhang *et al.* 2004).

Along the India-Eurasia Plate boundary in the Indo-Burma ranges, input horizontal convergence rates are at $\sim 5 \pm 5 \text{ mm a}^{-1}$. Our preferred model gives an output horizontal convergence rate of $3\text{--}5 \text{ mm a}^{-1}$.

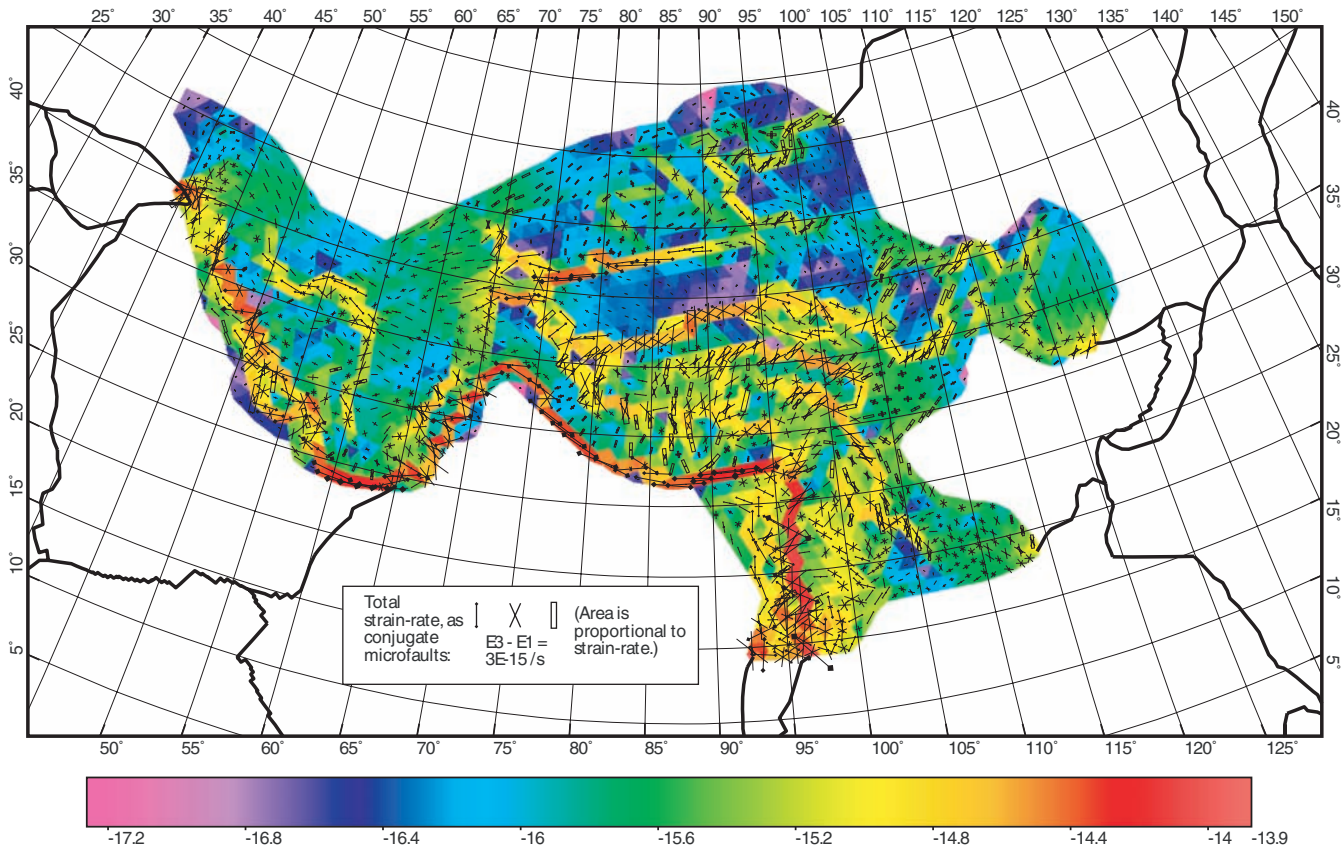


Figure 9. Total long-term-average anelastic strain-rate field (including faulting) of preferred model PTB2007008. Coloured background shows common logarithm of the magnitude of the principal strain rate which has the greatest magnitude. Overlying icons show total strain rate tensor (expressed as microfault orientations): dumbbell symbols show conjugate thrust faulting; X symbols show conjugate strike-slip faulting; rectangles show conjugate normal faulting. The fault symbols are sized with area proportional to strain-rate. To increase legibility, tensor icons are plotted for only 1/2 of the finite elements.

Table 2. Contrasting model predictions of heave rates (mm a^{-1}) of selected faults in some^a recent models.

| Fault | Elastic microplate models | | Deforming-continuum model This study |
|-------------------|---------------------------|-----------------------------|---|
| | Thatcher (2007) | Meade (2007) | |
| Altyn Tagh | 8–9 | 5–8 | 13 |
| Burman Ranges | | 31–49 (includes Sagaing) | 3–5 |
| Chaman | | | 2–22 |
| Himalayan Frontal | | 17–21 | 11–20 |
| Jiali | | 4–15 | 10 |
| Karakax | | | 4–8 |
| Karakorum | | 4–5 | 4–5 |
| Kunlun | 6–7 | 11–12 | 6–12 |
| Longmenshan | | | –2 |
| Sagaing | | See Burman Ranges | 22–35 |
| Tien Shan | | 5–11 | 3–14 |
| Xianshuihe | 8–12 | 9 | 5–15 |

^aNeither Holt *et al.* (2000) nor England & Molnar (2005) computed *a posteriori* (output) heave rates or slip rates on faults.

Our preferred model estimates (output) slip rates of $\sim 10 \text{ mm a}^{-1}$ on several dextral strike-slip faults in central Tibet. To the north, numerous sinistral strike-slip faults are estimated to have $2\text{--}3 \text{ mm a}^{-1}$ of slip-rate each, with total slip rate of $\sim 11 \text{ mm a}^{-1}$. The

large output slip rates of $\sim 10 \text{ mm a}^{-1}$ on a few dextral strike-slip faults in southcentral Tibet, such as the Jiali fault, may be caused by our inadequate representation of fault networks in the interior of Tibet. Field studies show pervasive conjugate strike-slip fault system spacing at 70–400 km (Taylor *et al.* 2003). If east–west extension is accommodated by these conjugate strike-slip faults in north and southcentral Tibet, the sum of slip rates yields an extension rate $\sim 20 \text{ mm a}^{-1}$, consistent with geodetic measurements (Jade *et al.* 2004).

Arabia–Eurasia relative plate motion in eastern Iran (east of $\sim 58^\circ\text{E}$) is mainly accommodated by the Makran subduction zone and Kopet Dagh. Despite little constraint from input geological slip rates, our model predicts the correct sense (compared to earthquake focal mechanisms) for strike-slip faults on the west and east sides of the Lut block. The central Iran and Lut blocks appear to be relatively rigid, with strain localization on their boundary faults. West of 58°E , Arabia–Eurasia convergence is accommodated by the Zagros and Alborz mountain ranges. Output slip rates of $\sim 16 \text{ mm a}^{-1}$ on the Main Recent fault are compatible with input slip rates of $10\text{--}17 \text{ mm a}^{-1}$ (Talebian & Jackson 2002) but much larger than geodetic slip rates of $3 \pm 2 \text{ mm a}^{-1}$ (Vernant *et al.* 2004). We suggest that a transition from strong to weak coupling between the underthrusting Arabia Plate and the Zagros in western Iran and Makran subduction in the east may affect surface deformation patterns in the Zagros and the Makran subduction zone. More constraints from GPS data and geological measurements and dynamic modelling would help understand these issues.

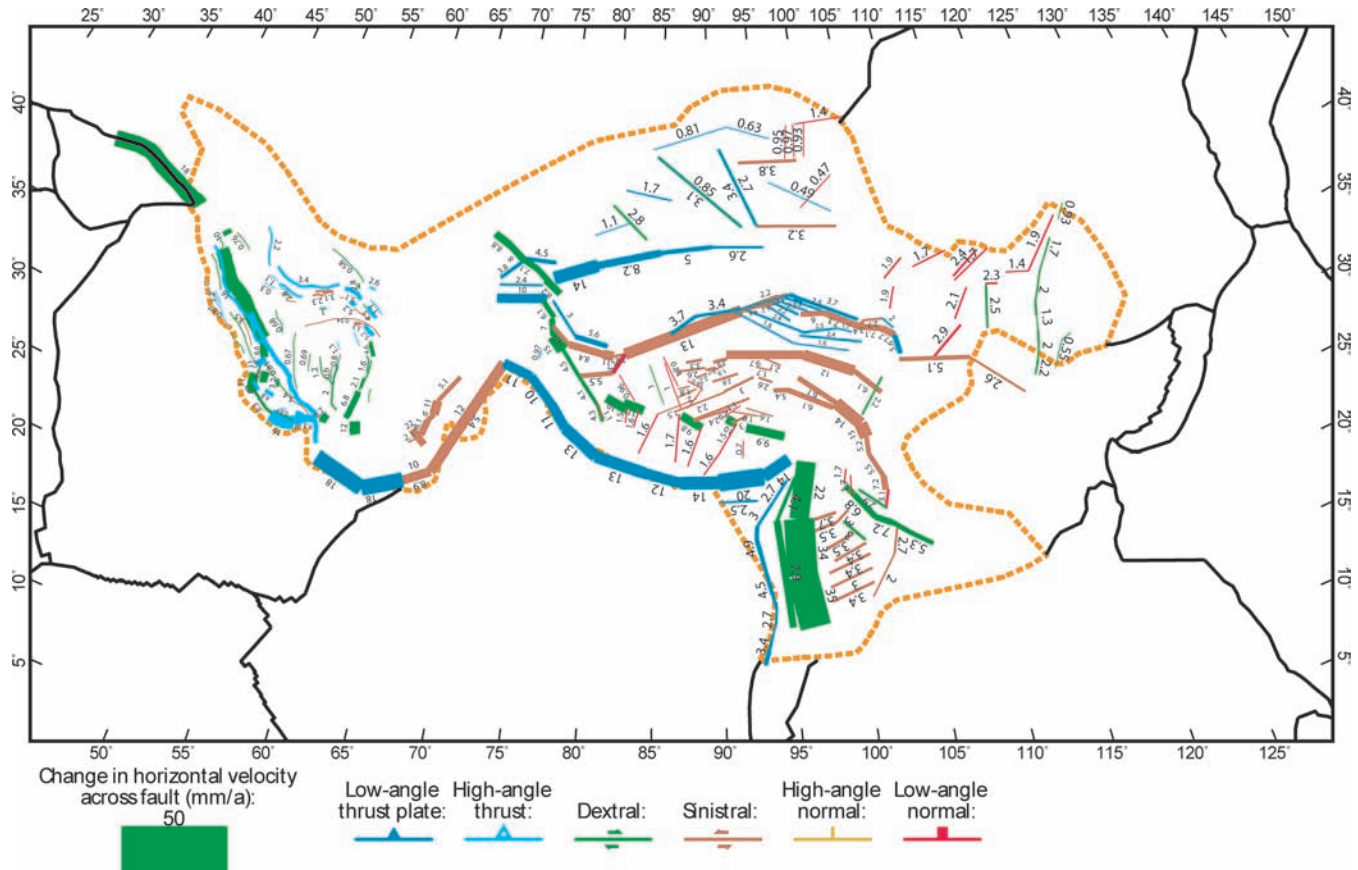


Figure 10. Posterior (output) best-estimate fault heave rates from model PTB2007008. The width of each ribbon plotted along a fault trace is proportional to long-term heave rate, which is also given by numbers in mm a^{-1} .

5 DISCUSSION AND APPLICATIONS

5.1 Decadal versus geological deformation

It is commonly assumed that geodetic velocities measured over years or decades are representative of velocities over geological timescales, although this claim is only occasionally tested. The discrepancy between geological and geodetic slip rates for some major strike-slip faults in central Asia indicates that either some estimates have uncertainties larger than those stated, or are based on erroneous interpretations, or that tectonic flow rates vary over time. We developed the NeoKinema method under an assumption that neither kind of data has any systematic bias, and that all uncertainties can be approximated by Gaussian distributions. If this were not true, we would expect to find that it is impossible to fit both classes of data with the same model. In fact, we find that our merged long-term-average velocity field provides a satisfactory fit to both geodetic velocities and geological heave rates (as did Holt *et al.* 2000), as well as to most-compressive horizontal principal stress/strain-rate directions at their respective uncertainty levels. This suggests that the tectonic flow over timescale of tens of years is not very different from tectonic flows over 10^4 – 10^6 yr, except in the zones of time-dependent elastic strain along major faults.

5.2 Deformation dynamics

Within this orogen our neotectonic flow solution shows a mixed deformation pattern, which includes continental collision at the

Himalayan front, a few semi-rigid blocks (e.g. Central Iranian and Lut blocks, South Caspian basin, Tarim basin, Gobi-Alashan block) within broadly distributed deformation, oceanic subduction zones (Makran) and transition zones between these elements.

Many dynamic models have been proposed to simulate the continental collision process between India and Eurasia and the evolution of Tibet. Typically they fall into two classes: block-like ‘extrusion’ models and thin viscous sheet models. As mentioned before, block-extrusion models have deformation accommodated by slip across a limited number of strike-slip faults of lithospheric scale, while the interiors of blocks are rigid. Our long-term-average velocity and strain-rate fields provide no support for rigid-block models of Tibet, as attested by significant horizontal contraction and extension rates inside the plateau.

In thin-viscous sheet models, the crust is treated as viscous or power-law fluid and undergoes continuous shortening and thickening under plate boundary forces and gravity (Houseman & England 1993). Shen *et al.* (2001) proposed a variant of the viscous sheet model, in which she considered viscosity variations with depth and concluded that significant channel flow would develop in the weak lower crust after formation of the Tibet plateau. This ‘channel flow’ model matches most features of our long-term deformation field in Tibet, especially around its southeastern margin and the Himalayan syntaxis. Lower crustal flow appears to be permitted by seismological evidence of low P - and S -wave velocities and high electrical conductivity in the Tibetan middle and lower crust (Curtis & Woodhouse 1997; Wei *et al.* 2001; Liu *et al.* 2005). It leads directly to the decoupling of upper crust and mantle. However, Flesch *et al.*

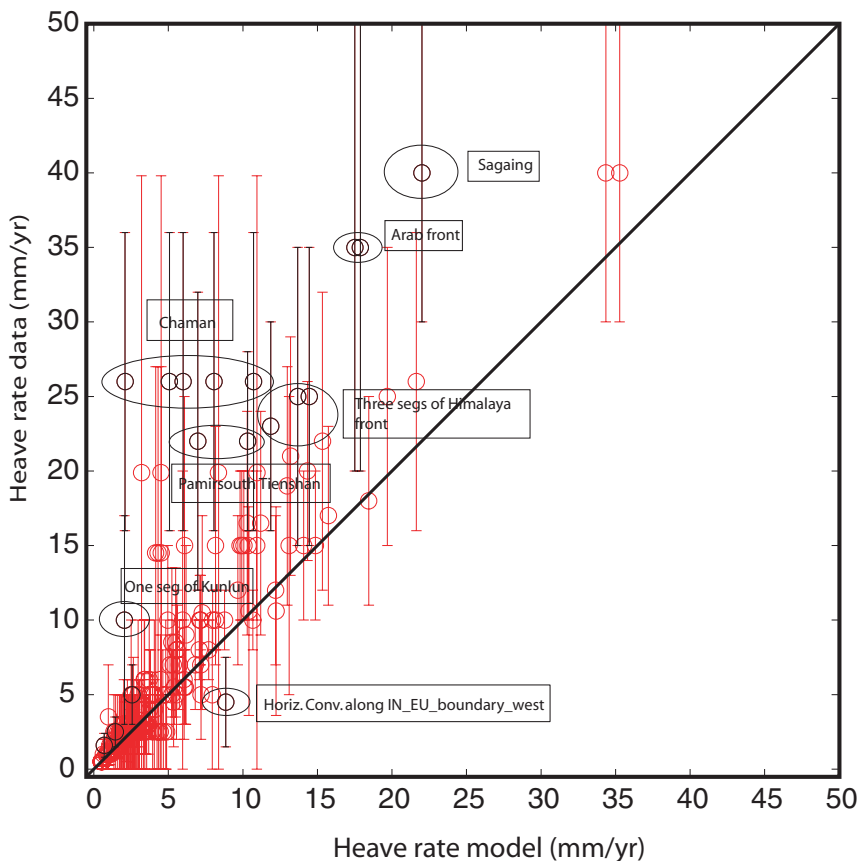


Figure 11. Prior (input) fault heave rates (vertical axis) versus posterior (output) fault heave rates (horizontal axis) from PTB2007008. Error bars show the minimum and maximum heave rates associated with input geological constraints. Faults that have no geological heave rate constraint are not shown. The diagonal line is the line along which output model heave rate is equal to input geological heave rate. For most faults, output heave rates lie within the error bounds of the input heave rates. Faults that do not have compatible rates are indicated as black circles (or sets of black circles, if the model fault is segmented) and error bars and their fault names are given.

(2005) argued, based on comparison of the surface strain-rate field with the strain of the mantle lithosphere inferred from SKS shear wave splitting, that the crust and mantle lithosphere are mechanically coupled and coherently deformed, and that the lower crust and mantle lithosphere have approximately the same strength. It is difficult to decide between these two models purely on the basis of empirical directional patterns, and very likely indirect evidence from thermal models and laboratory rock mechanics will need to play a role.

Nevertheless, our results on patterns of present shortening-rate directions may be helpful to some extent. Fig. 12 shows the most-compressive horizontal principal strain-rate axes of preferred model PTB2007008 versus interpolated stress/strain-rate directions. At 65–110°E, the model most-compressive principal strain-rate axes are roughly perpendicular to the India-Eurasia Plate boundary, and fan out over large distances, except where they rotate N–S or southward near the southeastern margins of Tibet. Similar patterns are seen in the Arabia-Eurasia collision zone in Iran. The nearly consistent principal strain-rate axis directions across topographic gradients such as that between Tibet and the Tarim basin suggests that long-wavelength plate boundary forces play a dominant role in determining crustal and mantle deformation, relative to local topographic forces and/or heterogeneities in strength (at least to the west of the southeastern margin of Tibet). Logically, flow fields that are dominated by distant lateral boundary conditions and rela-

tively insensitive to local heterogeneities might be expected to develop similar patterns at the upper-crustal and mantle-lithosphere levels. It is possible to reconcile shear wave splitting measurements with a ‘channel flow’ model if lateral velocity boundary conditions applied to both layers cause mantle-lithosphere deformation to be parallel to surface deformation (Holt 2000). Admittedly, extensive dynamic modelling will be needed to test this hypothesis; Flesch *et al.* (2005) were unable to make such models succeed in their attempts.

If much of the crust beneath central Asia is deforming by large-scale lower crustal flow in response to India’s collision with Eurasia, the semi-rigid blocks identified in our long-term-average strain and velocity fields would be at the upper-crustal level, effectively decoupled from underlying mantle lithosphere, and acting as lateral strength heterogeneities embedded in a broadly distributed deforming zone. In this view, faults in the strong upper crust may still localize the strain, but to a lesser degree than in models with lithospheric-scale boundary faults between rigid blocks. This view may also be applicable to other deforming regions such as the Zagros fold-and-thrust belt in Iran, as suggested by Jackson *et al.* (1995). Chen *et al.* (2004) proposed a deforming-block model for central Tibet. As noted by Shen *et al.* (2005) who studied the southeastern margin of the plateau, with ever-decreasing sizes of blocks, block models become indistinguishable from distributed deformation models.

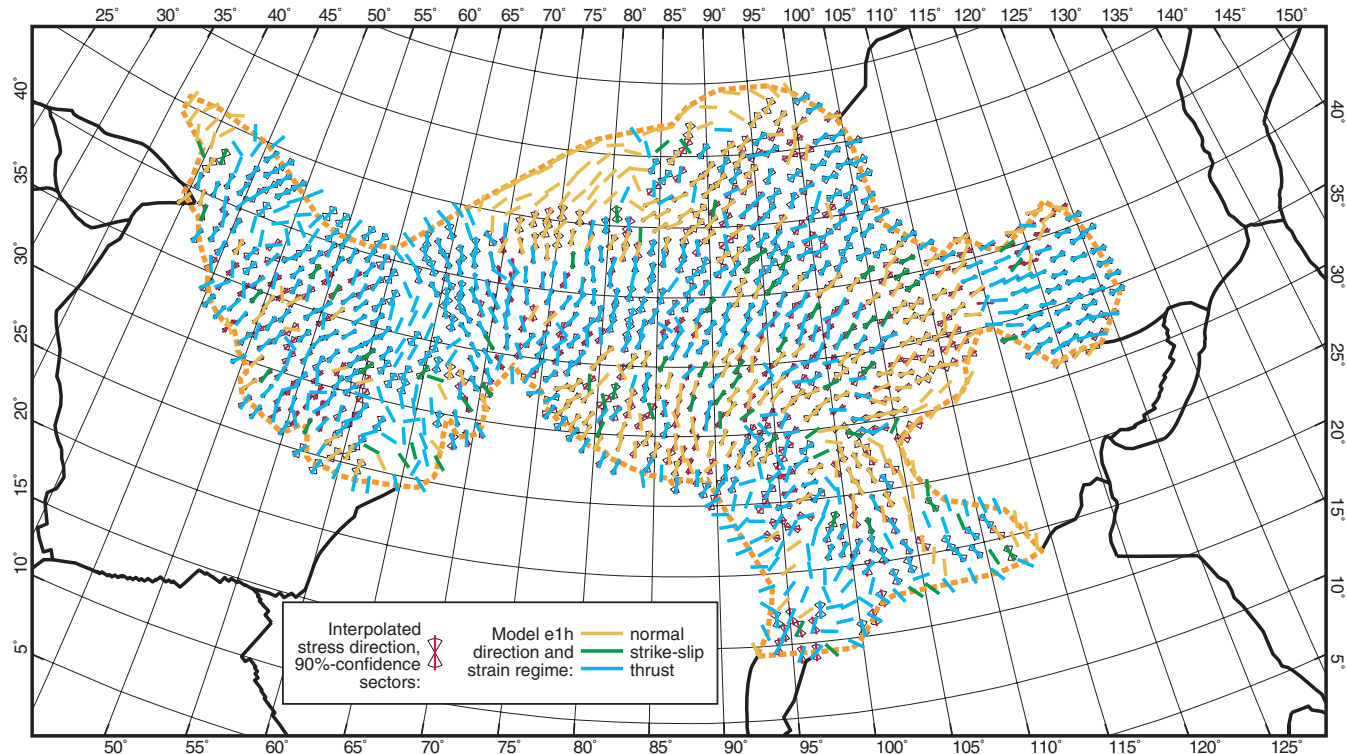


Figure 12. Most-compressive horizontal principal strain-rate axes predicted by the preferred model PTB2007008 (on top). Underlying (and frequently hidden) are interpolated ‘stress directions’ with 90 per cent confidence-bounds (as in Fig. 4). Intentional overplotting of the input field by the output field de-emphasizes regions where the model performed as requested, and emphasizes regions where it was unable to conform principal strain-rate axes to the requested azimuths. Only ‘stress directions’ with 90 per cent confidence-fans of $\pm 45^\circ$ or less are plotted, as these are the only interpolated ‘stress directions’ that are used as constraints in NeoKinema. The fanning-out of principal strain-rate axes perpendicular to the margin of India–Eurasia boundary over large distances suggests that plate-boundary driving forces play an dominant role in the deformation of central Asia.

5.3 Long-term seismicity inferred from tectonics

It is possible to compute a stationary long-term model of seismicity based almost entirely on tectonic flow. The hypotheses and algorithms were detailed by Bird & Liu (2007), where they were referred to collectively by the acronym SHIFT (Seismic Hazard Inferred From Tectonics). Long-term seismic moment rates (per unit of surface area) are first estimated from the derivatives and discontinuities in the tectonic velocity field, in map view. Then, long-term average shallow (depth < 70 km) seismicity is calculated from this long-term seismic moment rate using an assumed magnitude-frequency distribution. All the necessary parameters (coupled seismogenic thickness, spectral slope β , and corner magnitude) were determined by Bird & Kagan (2004) for each type of plate boundary, and the essential hypothesis of the SHIFT method is that any deforming region can be treated as a small patch of the ‘most comparable’ type of plate boundary. Note that such a long-term-average seismicity map is stationary, or virtually independent of time. We hope it will be more reliable than those that are based primarily on short instrumental earthquake catalogues and/or longer, but very incomplete, historical records.

For any discrete fault, the long-term average seismic moment rate is calculated using

$$\dot{M}_0 \cong \langle cz \rangle \int G \sqrt{v_p^2 + [v_o \sec(\theta)]^2} \csc(\theta) d\ell,$$

where \dot{M}_0 is the seismic moment rate (N m s^{-1}) of the fault, $\langle cz \rangle$ represents mean coupled seismogenic thickness, θ is the fault dip, G is the shear modulus and v_p and v_o are the trace-parallel and

orthogonal components of the horizontal relative velocity vector. The integral is taken on the surface, along the trace of the fault. The mean coupled seismogenic thickness $\langle cz \rangle$ is assigned using values inferred for most comparable type of plate boundary in the global study of Bird & Kagan (2004).

For anelastic deforming continua that lies between modelled faults, the seismic moment production of an area A of lithosphere with uniform long-term anelastic strain rate tensor is

$$\dot{M}_0 = A \langle cz \rangle G \begin{cases} 2\dot{\varepsilon}_3; & \text{if } \dot{\varepsilon}_2 < 0, \text{ or} \\ -2\dot{\varepsilon}_1; & \text{if } \dot{\varepsilon}_2 \geq 0 \end{cases},$$

where $\dot{\varepsilon}_1$, $\dot{\varepsilon}_2$, $\dot{\varepsilon}_3$ are principal values of the anelastic strain-rate tensor with ordering $\dot{\varepsilon}_1 \leq \dot{\varepsilon}_2 \leq \dot{\varepsilon}_3$. Depending on the crustal type (continental or oceanic) and the magnitude of the vertical principal strain rate relative to the two horizontal principal strain rates, an appropriate plate boundary analogue is determined and associated $\langle cz \rangle$ and shear modulus G are found in tables. Once long-term seismic moment rate is known, we obtain long-term seismicity rate by using the tapered Gutenberg–Richter model of the frequency/moment relation (Kagan 2002), again taking the necessary parameters (spectral slope β , and corner magnitude) from the results of Bird & Kagan (2004) for the ‘most comparable’ type of plate boundary.

Fig. 13 shows a map of the logarithm of our long-term forecast seismicity (including aftershocks) above threshold magnitude 5.67 within the shallow depth range of 0–70 km. Note that relative plate velocities used to compute plate-boundary seismicity outside the Persia–Tibet–Burma orogen are from the rigid-plate PB2002

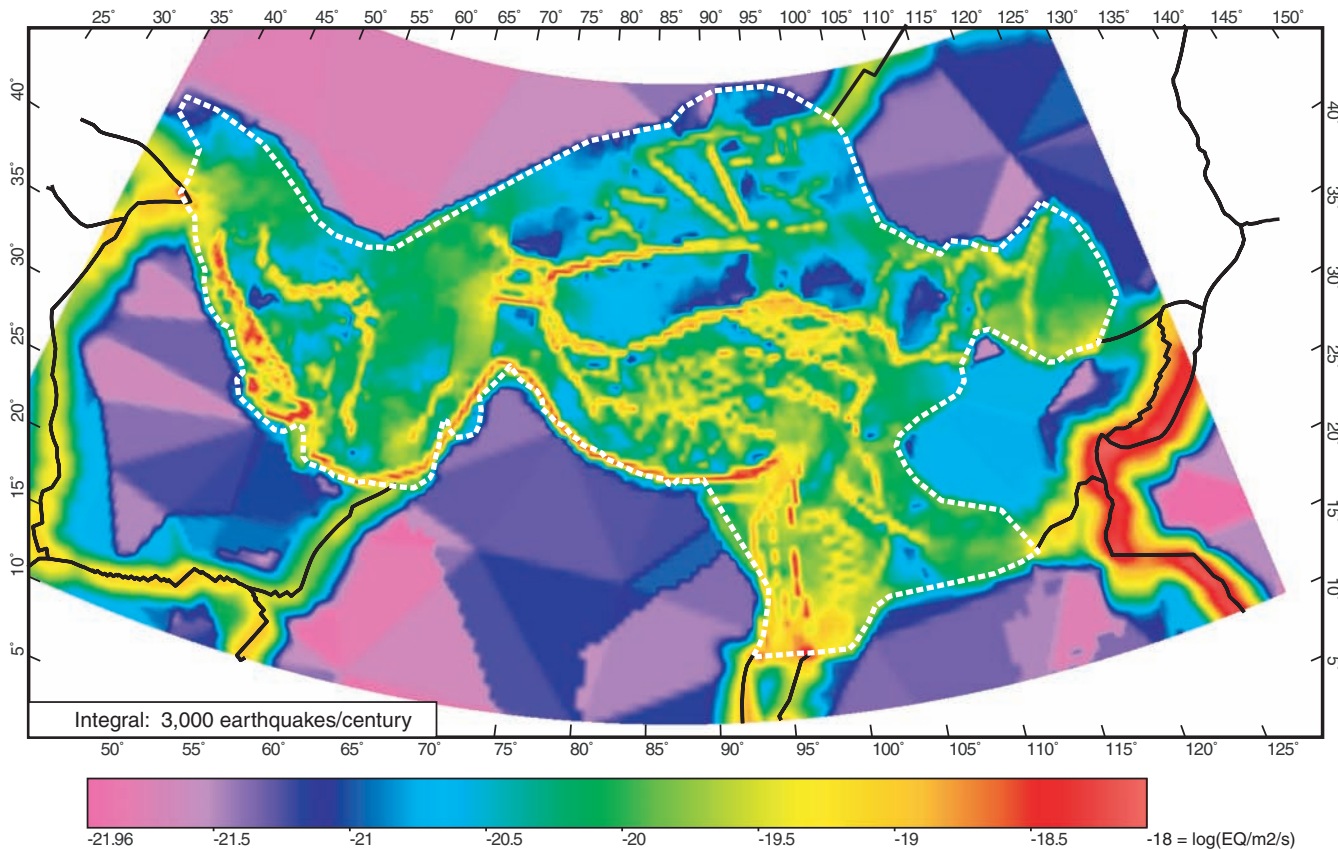


Figure 13. Common logarithm of forecast long-term seismicity (in epicentres per square metre per second, including aftershocks) in the Persia–Tibet–Burma orogen for threshold magnitude 5.67, evaluated on a 0.5-degree grid. Based on kinematics from NeoKinema model PTB2007008. Intraplate seismicity outside the orogen is based on strain rates from Shells model i2000-01 with mesh grid Earth2P.feg (Bird 1998). Plate-boundary seismicity outside the orogen is based on rigid-plate model PB2002 of Bird (2003). The spatial integral (across the entire coloured ‘rectangle’) of the forecast rate is 772 per 25.75 yr (or 3000 per century) in the depth range 0–70 km. The spatial integral in the orogen (indicated by the heavy dashed line) of the forecast rate is 371 per 25.75 yr (or 1441 per century) in the depth range 0–70 km.

model of Bird (2003), while intraplate strain rates used to compute intraplate seismicity outside the Persia–Tibet–Burma orogen are from a dynamic thin-shell F-E model by Bird (1998) (Shells model 2000–2001 with mesh grid Earth2P.feg). (The contribution of the latter is small and will not be discussed here.)

Actual seismicity from the Harvard CMT catalogue with the same magnitude threshold and depth range during 1977 January–2002 September is overlaid in Fig. 14. Generally, earthquakes tend to fall in predicted high-seismicity zones (e.g. Zagros fold-and-thrust belt, transpressive eastern boundary faults of Helmand, Chaman, Pamir south and west Tianshan, north and south margins of Tibet, Indo-Burma range and southeast borderland of the Tibet plateau). There are also regions which had little or no seismicity (as forecast) such as the Tarim basin, Gobi platform, Ordos block, Dzunggar basin, Kazakh, Helmand block, central Iran and Lut blocks and South Caspian basin. In general the observed seismicity is spatially consistent with the stationary forecast.

The primary discrepancies between the seismicity model and the catalogue lie along the Himalayan frontal fault system, the faults of the High Zagros Mountains and the Altyn Tagh fault. In all of these cases, the large number of $m > 5.67$ earthquakes expected did not occur during 1977–2002.

It is easy to integrate the model seismicity rate across the map, in order to compare gross quantitative statistics. Within the Persia–Tibet–Burma orogen (heavy dashed curve) where tectonic flow was

modelled with NeoKinema, the SHIFT forecast is for 371 $m > 5.67$ earthquakes in any period of 25.75 yr, which exceeds the Harvard CMT catalogue count of 238 during 1977 January–2002 September. (In the larger geographic ‘rectangle’ 10–55°N, 35–130°E which is coloured in the figures, the model forecast is for 772 $m > 5.67$ earthquakes per 25.75 yr, also exceeding the Harvard CMT catalogue count of 536 for the same period.)

If earthquakes were independent events, so that the number of events detected in a fixed spatial/temporal window was described by the binomial distribution, then the chances of getting such different counts as 371 and 238 in two samples from the same population would be vanishingly small. We would have to conclude that some aspect(s) of our tectonic-flow model, and/or of the SHIFT hypothesis, is/are wrong. Perhaps the weakest link is our assumption that all continental convergent boundaries have the same coupled seismogenic thickness.

However, it is well established that earthquakes are strongly clustered in both space and time, although the appropriate distributions to describe these phenomena have not been worked out for large earthquakes and long time windows (only for aftershocks). This means that the level of significance of the discrepancy between 371 earthquakes (forecast) and 238 earthquakes (observed) is still unclear. It may be that such discrepancies are a common result of stochastic time-dependence in an epidemic-type or Markov-chain-type process.

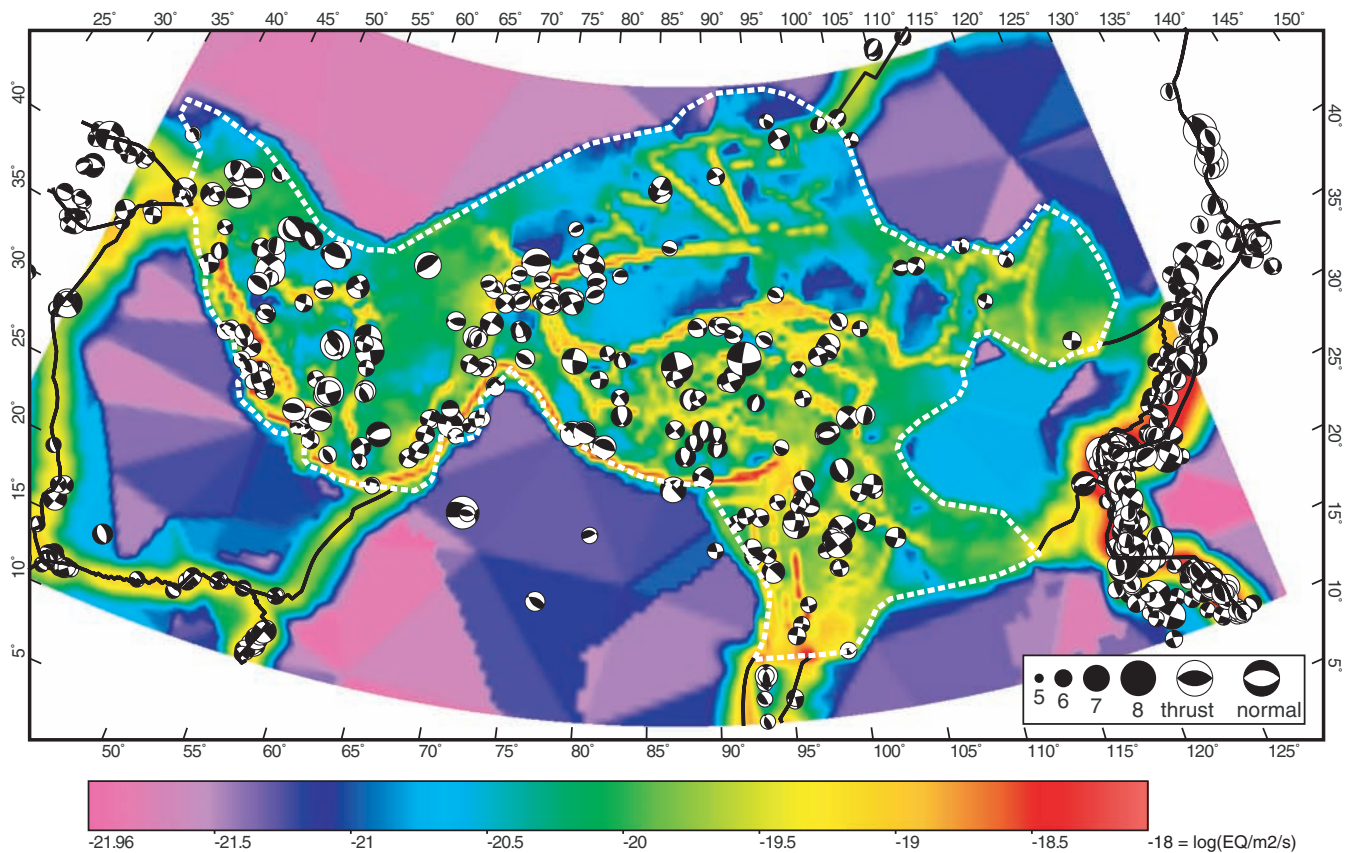


Figure 14. Common logarithm of forecast long-term seismicity is shown by the colour map. (See Fig. 13 for details.) For comparison, $m > 5.67$ earthquakes from the Harvard CMT catalogue with depths of 0–70 km during 1997.01–2002.09 are shown as double-couple moment tensors projected on lower focal hemispheres. There are 238 earthquakes within the orogen, plus an additional 298 earthquakes outside the orogen but within the coloured ‘rectangle’ (total 536). Additional earthquakes shown outside the coloured areas are not included in these counts.

If the discrepancy is due to time-dependence, this could have occurred in the orogen, in the external population used for calibration of continental convergent boundary seismicity, or both. The Persia–Tibet–Burma orogen is so large that it encompasses about 46 per cent of the continental convergent boundaries on Earth (CCB’s of Bird 2003 and of Bird & Kagan 2004). Therefore, the count of shallow CCB earthquakes, outside orogens, which Bird and Kagan used to calibrate CCB seismicity was only 259 during a similar time window, also using the Harvard CMT catalogue. Perhaps this number exceeds the true long-term average due to aftershock swarms in the calibration regions.

The third possibility is that earthquake activity in the Persia–Tibet–Burma orogen may have been below its long-term seismicity level during 1977–2002 due to lack of large earthquakes along the Himalayan frontal thrust fault zone, Altyn Tagh fault and High Zagros. It has been frequently stated that the Himalayan frontal fault system can and will produce great earthquakes in spite of its relative quiescence during the CMT catalogue period (Triep & Sykes 1997; Cattin & Avouac 2000; Rong 2002; Rong & Jackson 2002; Bilham 2004; Kumar *et al.* 2006). This is supported by slip-deficit buildup at a rate of $\sim 14 \text{ mm a}^{-1}$ along its northwest segment inferred from geodetic observations (Banerjee & Burgmann 2002). According to typical scaling in continental convergent boundaries (Bird & Kagan 2004), a single magnitude 8.0 event might eventually stimulate as many as 100–170 total aftershocks with $m > 5.67$, which would nearly ‘correct’ the discrepancy. The great ($m = 9.0$) Sumatra–Andaman earthquake of 2004.12.26 was admittedly

in a different tectonic setting, but it generated 250 aftershocks large enough to be recorded in the Harvard CMT catalogue in the first 11 months (Gibowicz & Debski 2006). Therefore, the discrepancy between our long-term forecast and actual 1997–2002 seismicity can be explained as a temporary, time-dependent deviation if one considers the Himalayan front capable of generating earthquakes of moment magnitude $\sim 8\text{--}9$. Considering the devastation caused by the $m = 7.6$ earthquake of 2005.10.08 in Kashmir (Fujiwara *et al.* 2006), this possibility must be taken very seriously.

Our long-term-average earthquake forecast provides an interesting estimate of future earthquake frequency which is based primarily on tectonics. Conclusive tests of its validity will probably require both better understanding of earthquake statistics, and also earthquake catalogues with longer time spans and/or larger regions. Until this testing is complete, it would be prudent to consider the tectonic forecast as a part of the range of plausible estimates when assessing seismic hazard and choosing social policies.

6 CONCLUSIONS

We use a kinematic finite-element method to derive a self-consistent long-term-average velocity field by combining space geodesy, geological slip rates and principal ‘stress directions’ (e.g. seismic moment tensor orientations). We find that, after bootstrap determination of continuum stiffness and adjustment of two tuning parameters, a single model can fit geodetic, geological and ‘stress direction’

data almost equally well. Our results suggest that regional anelastic deformation over tens of years is not (yet) distinguishable from anelastic deformation over neotectonic timescales (10^4 – 10^6 yr). The detailed deformation pattern within the orogen can be described as a mixed pattern, in which semi-rigid blocks (e.g. Tarim basin, Ordos, ...) are embedded in a distributed deformation zone. However, the high mean anelastic strain-rate (0.7 per cent Ma^{-1}) which we infer in the continuum between major faults implies that the orogen should not be modelled as a set of rigid microplates. The long-wavelength consistency of principal strain-rate axes and modest slip rates on the boundary faults of the few semi-rigid blocks suggest that they are acting as crustal heterogeneities modulating underlying distributed deformation. We compute a map of estimated long-term-average seismicity which (unlike instrumental seismicity in 1977–2002) forecasts many events along the Himalayan frontal faults, High Zagros and Altyn Tagh zones. This long-term seismicity map may provide useful guidance for seismic zoning and earthquake hazard reduction in the region. An overall discrepancy between the forecast and observed levels of seismicity remains an important problem for future research.

ACKNOWLEDGMENT

We thank Z.K. Shen for providing us with collected GPS data, Michael Taylor and Bernard Guest for illuminating discussion on regional tectonics. The paper also benefits greatly from the careful reviews of associate editor John Beavan, Philip England and an anonymous reviewer. This material is based upon work supported by the National Science Foundation under Grant Number EAR-0336950.

REFERENCES

- Armijo, R., Tapponnier, P. & Han, T.L., 1989. Late Cenozoic right lateral strike-slip faulting in southern Tibet, *J. geophys. Res.*, **94**, 2787–2838.
- Avouac, J.P. & Tapponnier, P., 1993. Kinematic model of active deformation in central Asia, *Geophys. Res. Lett.*, **20**, 895–898.
- Banerjee, P. & Burgmann, R., 2002. Convergence across the northwest Himalaya from GPS measurements, *Geophys. Res. Lett.*, doi:10.1029/2002GL015184.
- Bayer R. et al., 2006. Active deformation in Zagros-Makran transition zone inferred from GPS measurements, *Geophys. J. Int.*, **165**, 373–381.
- Bendick, R., Bilham, R., Freymueller, J., Larson, K. & Yin, G., 2000. Geodetic evidence for a low slip rate in the Altyn Tagh fault system, *Nature*, **404**, 69–72.
- Berberian, M. & Yeats, R.S., 2001. Contribution of archaeological data to studies of earthquake history in the Iranian Plateau, *J. Struct. Geol.*, **23**, 563–584.
- Bilham, R., 2004. Earthquakes in India and the Himalaya; tectonics, geodesy and history, *Annal. Geophys.*, **47**(2/3), 839–858.
- Bird, P., 1998. Testing hypotheses on plate-driving mechanisms with global lithosphere models including topography, thermal structure, and faults, *J. geophys. Res.*, **103**(B5), 10 115–10 129.
- Bird, P., 2003. An updated digital model of plate boundaries, *Geochem., Geophys., Geosys.*, **4**(3), doi:10.1029/2001GC000252.
- Bird, P. & Kagan, Y.Y., 2004. Plate-Tectonic analysis of shallow seismicity: apparent boundary width, beta, corner magnitude, coupled lithosphere thickness, and coupling in seven tectonic settings, *Bull. seism. Soc. Am.*, **94**(6), 2380–2399.
- Bird, P. & Li, Y., 1996. Interpolation of principal stress directions by non-parametric statistics: global maps with confidence limits, *J. geophys. Res.*, **101**, 5435–5443.
- Bird, P. & Liu, Z., 2007. Seismic hazard inferred from tectonics: California, *Seismol. Res. Lett.*, **78**, 37–48.
- Brown, E.T., Bendick, R., Bourles, D.L., Gaur, V., Molnar, P., Raisbeck, G.M. & Yiou, F., 2002. Slip rates of the Karakorum fault, Ladakh, India, determined using cosmic ray exposure dating of debris flows and moraines, *J. geophys. Res.*, **107**(B9), 2192, doi:10.1029/2000JB0001000.
- Cattin, R. & Avouac, J.P., 2000. Modeling mountain building and the seismic cycle in the Himalaya of Nepal, *J. geophys. Res.*, **105**, 13 389–13 407.
- Chen, Z. et al., 2000. Global Positioning System measurements from eastern Tibet and their implications for India/Eurasia intercontinental deformation, *J. geophys. Res.*, **105**, 16 215–16 227.
- Chen, Q.Z., Freymueller, J.T., Wang, Q., Yang, Z., Xu, C. & Liu, J., 2004. A deforming block model for the present-day tectonics of Tibet, *J. geophys. Res.*, **109**, B01403, doi:10.1029/2002JB002151.
- Chamot-Rooke, N. & Le Pichon, X., 1999. GPS determined eastward Sundaland motion with respect to Eurasia confirmed by earthquakes slip vectors at Sunda and Philippine trenches, *Earth Planet. Sci. Lett.*, **173**, 439–455.
- Curtis, A. & Woodhouse, J., 1997. Crust and upper mantle shear velocity structure beneath the Tibetan plateau and surrounding region from interevent surface wave phase velocity inversion, *J. geophys. Res.*, **102**, 11789–11813.
- DeMets, C., Gordon, R.G., Argus, D.F. & Stein, S., 1994. Effects of recent revisions to the geomagnetic reversal time scale on estimates of current plate motions, *Geophys. Res. Lett.*, **21**(20), 2191–2194.
- England, P.C. & Molnar, P., 1997. The field of crustal velocity in Asia calculated from Quaternary rates of slip on faults, *Geophys. J. Int.*, **130**, 551–582.
- England, P.C. & Molnar, P., 2005. Late Quaternary to decadal velocity fields in Asia, *J. geophys. Res.*, **110**, B12401, doi:10.1029/2004JB003541.
- Flesch, L.M., Holt, W.E., Silver, P.G., Stephenson, M., Wang, C.-Y. & Chan, W.W., 2005. Constraining the extent of crust-mantle coupling in central Asia using GPS, geologic, and shear wave splitting data, *Earth Planet. Sci. Lett.*, **238**, 24–268.
- Fujiwara, S. et al., 2006. Satellite data gives snapshot of the 2005 Pakistan earthquake, *Eos Trans. AGU*, **87**(7), 73–77.
- Gibowicz, S.J. & Debowski, W., 2006. Seismicity before and after the two great Sumatra earthquakes of 2004 and 2005, *Acta Geophys.*, **54**(4), 343–360, doi:10.2478/s11600-006-0028-5.
- Holt, W.E., 2000. Correlated crust and mantle strain fields in Tibet, *Geology*, **28**(1), 67–70.
- Holt, W.E., Chamot-Rooke, N., Le Pichon, X., Haines, A.J., Shen-Tu, B. & Ren, J., 2000. Velocity field in Asia inferred from Quaternary fault slip rates and Global Positioning System observations, *J. geophys. Res.*, **105**(B8), 19 185–19 209.
- Houseman, G. & England, P., 1993. Crustal thickening versus lateral expulsion in Indian-Asian continental collision, *J. geophys. Res.*, **98**, 12 233–12 249.
- Hubert-Ferrari, A., Rolando, A., King, G., Meyer, B. & Barka, A., 2002. Morphology, displacement, and slip rates along the North Anatolian Fault, Turkey, *J. geophys. Res.*, **107**(10), 2235, doi:10.1029/2001JB000393.
- Jackson, J., Haines, J. & Holt, W., 1995. The accommodation of Arabia-Eurasia plate convergence in Iran, *J. geophys. Res.*, **100**(B8), 15 205–15 219.
- Jade, S., Bhatt, B.C., Yang, Z., Bendick, R., Gaur, V.K., Molnar, P., Anand, M.B. & Kumar, D., 2004. GPS measurements from the Ladakh Himalaya, India: preliminary tests of plate-like or continuous deformation in Tibet, *GSA Bull.*, **116**(11/12), 1385–1391, doi:10.1130/B25357.
- Kagan, Y.Y., 2002. Seismic moment distribution revisited: II. Moment conservation principle, *Geophys. J. Int.*, **149**, 731–754.
- Kong, X. & Bird, P., 1995. SHELLS: a thin-shell program for modeling neotectonics of regional or global lithosphere with faults, *J. geophys. Res.*, **100**, 22 129–22 131.
- Kreemer, C. & Holt, W.E., 2001. A no-net-rotation model of present-day surface motions, *Geophys. Res. Lett.*, **28**(23), 4407–4410.
- Kreemer, C., Holt, W.E., Haines, A.J., 2003. An integrated global model of present-day plate motions and plate boundary deformation, *Geophys. J. Int.*, **154**, 8–34.

- Kumar, S., Wesnousky, S. G., Rockwell, T.K., Briggs, R.W., Thakur, V.C. & Jayangondaperumal, R., 2006. Paleoseismic evidence of great surface rupture earthquakes along the Indian Himalaya, *J. geophys. Res.*, **111**(B3), B03304, doi:10.1029/2004JB003309.
- Liu, Z. & Bird, P., 2002. Finite element modeling of neotectonics in New Zealand, *J. geophys. Res.*, **107**(B12), 2328, doi:10.1029/2001JB001075.
- Liu, Y., Chang, C., He, J., Liu, F. & Sun, H., 2005. Three-dimensional velocity images of the crust and upper mantle beneath the north-south zone in China, *Bull. seism. Soc. Am.*, **95**, 916–925.
- McClusky, S. et al., 2000. GPS constraints on plate motions and deformations in eastern Mediterranean and Caucasus, *J. geophys. Res.*, **105**, 5695–5719.
- McClusky, S., Reilinger, R., Mahmoud, S., Ben Sari, D. & Tealeb, A., 2003. GPS constraints on Africa(Nubia) and Arabia plate motions, *Geophys. J. Int.*, **155**, 126–138.
- Meade, B., 2007. Present-day kinematics at the India-Asia collision zone, *Geology*, **35**(1), 81–84, doi:10.1130/G22924A.1.
- Molnar, P., Fitch, T.J. & Wu, F.T., 1973. Fault plane solutions of shallow earthquakes and contemporary tectonics in Asia, *Earth Planet. Sci. Lett.*, **19**(2), 101–112.
- Murphy, M.A., Yin, A., Kapp, P., Harrison, T.M., Lin, D. & Jinghui, G., 2000. Southward propagation of the Karakorum fault system, southwest Tibet: timing and magnitude of slip, *Geology*, **28**, 451–454.
- Peltzer, G. & Saucier, F., 1996. Present-day kinematics of Asia derived from geologic fault rates, *J. geophys. Res.*, **101**, 27 943–27 956.
- Peltzer, G., Socquet, A., Lasserre, C., Meriaux, A., Tapponnier, P. & Ryerson, R., 2006. InSAR observations of interseismic strain along the central Altyn Tagh fault consistent with Holocene slip-rate, *Eos Trans. AGU*, **87**(52), Fall Meet. Suppl., Abstract T21E-02.
- Pollastro R.M., Karshbaum, A.S. & Viger, R.J., 1998. Map showing geology, oil and gas fields, and geologic provinces of Iran: U.S. Geological Survey Open File Report 97-470G, one CD-ROM.
- Rangin, C. et al., 1999. Plate convergence measured by GPS across the Sundaland/Philippine Sea plate deformed boundary: the Philippines and eastern Indonesia, *Geophys. J. Int.*, **139**, 296–316.
- Reinecker, J., Heidbach, O. & Mueller, B., 2003. The 2003 release of the World Stress Map (available online at www.world-stress-map.org).
- Rong, Y.-F., 2002. Evaluation of earthquake potential in China, *PhD dissertation*. University of California, Los Angeles.
- Rong, Y.-F. & Jackson, D.D., 2002. Earthquake potential in and around China: estimated from past earthquakes, *Geophys. Res. Lett.*, **29**(16), 1780, doi:10.1029/2002GL015297.
- Sella, G.F., Dixon, T.H. & Mao, A., 2002. REVEL: a model for recent plate velocities from space geodesy, *J. geophys. Res.*, **95**, 4873–4879.
- Shen, Z.K., Jackson, D.D. & Ge, B.X., 1996. Crustal deformation across and beyond the Los Angeles basin from geodetic measurements, *J. geophys. Res.*, **101**, 27 957–27 980.
- Shen-Tu, B. & Holt W.E., 1999. Deformation kinematics in the western United States determined from Quaternary fault slip rates and recent geodetic data, *J. geophys. Res.*, **104**(B12), 28 927–28 955.
- Shen, Z.K., Zhao, C.K., Yin, A., Li, Y.X., Jackson, D.D., Fang, P. & Dong, D., 2000. Contemporary crustal deformation in east Asia constrained by Global Positioning System measurements, *J. geophys. Res.*, **105**(B3), 5721–5734.
- Shen, F., Royden, L.H. & Burchfiel, B.C., 2001. Large-scale crustal deformation of the Tibetan Plateau, *J. geophys. Res.*, **106**(B4), 6793–6816.
- Shen, Z.K., Lu, J.N., Wang, M. & Burgmann, R., 2005. Contemporary crustal deformation around the southeast borderland of the Tibetan Plateau, *J. geophys. Res.*, **110**, B11409, doi:10.1029/2004JB003421.
- Socquet, A., Vigny, C., Chamot-Rooke, N., Simons, W., Rangin, C. & Ambrosius, B., 2006. India and Sunda plates motion and deformation along their boundary in Myanmar determined by GPS, *J. geophys. Res.*, **111**, B05406, doi:10.1029/2005JB003877.
- Talebian, M. & Jackson, J., 2002. Offset on the main recent fault of NW Iran and implications for the late Cenozoic tectonics of the Arabia-Eurasia collision zone, *Geophys. J. Int.*, **150**, 422–439.
- Taylor, M., Yin A., Ryerson, F.J., Kapp, P. & Ding, L., 2003. Conjugate strike-slip faulting along the Bangong-Nujiang suture zone accommodates coeval east-west extension and north-south shortening in the interior of the Tibetan Plateau, *Tectonics*, **22**(4), 1044, doi:10.1029/2002TC001361.
- Tatar, M., Hatzfeld, D., Martinod, J., Walpersdorf, A., Ghafori-Ashtiani, M., & Chery, J., 2002. The present-day deformation of the central Zagros from GPS measurements, *Geophys. Res. Lett.*, **29**, 19, 1927, doi:10.1029/2002GL015427.
- Thatcher, W., 2007. Microplate model for the present-day deformation of Tibet, *J. geophys. Res.*, **112**(B01), doi:10.1029/2005JB004244, 2007.
- Triep, E.G. & Sykes, L.R., 1997. Frequency of occurrence of moderate to great earthquakes in intracontinental regions: implications for changes in stress, earthquake prediction, and hazards assessment, *J. geophys. Res.*, **102**(B5), 9923–9948.
- Vernant, P. et al., 2004. Contemporary crustal deformation and plate kinematics in middle east constrained by GPS measurements in Iran and northern Oman, *Geophys. J. Int.*, **157**, 381–398, doi:10.1111/j.1365-246x.2004.0222.x.
- Walker, R. & Jackson, J., 2002. Offset and evolution of the Gowk fault, S. E. Iran: a major intra-continental strike-slip system, *J. Struct. Geol.*, **24**, 1677–1698.
- Wei, W. et al., 2001. Detection of widespread fluids in the Tibetan Crust by Magnetotelluric studies, *Science*, **292**, 5517, 716–719.
- Wang, Q. et al., 2001. Present-day crustal deformation in China constrained by global positioning system measurements, *Science*, **294**, 574–577.
- Wang, M., Shen, Z.K., Niu, Z.J., Zhang, Z.S., Sun, H.R., Gan, W.J., Wang, Q. & Ren, Q., 2003. Contemporary crustal deformation of Chinese continent and tectonic block model, *Science in China (series D)*, **46**, 25–40.
- Wright, T.J., Parsons, B., England, P.C. & Fielding, E.J., 2004. InSAR observations of low slip rates on the major faults of western Tibet, *Science*, **305**, 236–239.
- Zhang, P.Z. et al., 2004. Continuous deformation of the Tibetan Plateau from global positioning system data, *Geology*, **32**(9), 809–812, doi:10.1130/G20554.

SUPPLEMENTARY MATERIAL

The following supplementary material is available for this article:

Appendix S1. A full description of NeoKinema.

Appendix S2. The FORTRAN90 source code for NeoKinema.

Appendix S3. All 457 models listed with L0, L1 and L2-norms for each data class.

This material is available as part of the online article from:

<http://www.blackwell-synergy.com/doi/abs/10.1111/j.1365-246X.2007.03640.x>

(this link will take you to the article abstract).

Please note: Blackwell Publishing is not responsible for the content or functionality of any supplementary materials supplied by the authors. Any queries (other than missing material) should be directed to the corresponding author for the article.